

Biocompatible Nanoplasmonic Probes for the Detection of Single Biomolecules

Joseph Doll, Department of Mechanical Engineering
Bioengineering H194, Honors Undergraduate Research
Submitted to Professor Luke P. Lee
University of California, Berkeley

September 14, 2005

Contents

1	Introduction	5
1.1	What are Nanoplasmonic Probes?	5
1.2	A Survey of Nanoplasmonic Probes	6
1.2.1	Colloidal Metal Nanoparticles	6
1.2.2	Gold Nanoshell	8
1.2.3	Nanocrescent	10
1.2.4	Semiconductor Quantum Dots	11
1.3	Applications of Nanoplasmonic Probes	13
1.3.1	Surface Enhanced Raman Spectroscopy	13
1.3.2	Proteomics	14
2	Theory	16
2.1	The Complex Dielectric Function	18
2.2	Surface Modes in Spheres, The Electrostatic Approximation	20
2.3	Formulation of the Helmholtz Equation	23
2.4	Surface Modes in Spheres, General Solution	25
2.5	Surface Modes in Infinite Cylinders	28
2.6	Propagating Surface Plasmon Polaritons in Thin Metal Films	30
3	Numerical Simulations	34
3.1	Software and Hardware Specifications	34
3.2	The Programming Interface	35
3.3	Nanocrescent Optical Properties	36
3.4	Parametric Study of the Gold Nanocrescent Absorption Peaks	41
3.5	Magnetically Modulated Nanocrescent	45
4	Experiments	47
4.1	High Speed Spectral Imaging of Nanoplasmonic Probe Arrays	47

5	Future Goals	53
A	Theoretical Calculations Code	55
A.1	OpticalData.m	55
A.2	ElectrostaticSpectra.m	58
A.3	SphereSpectra.m	59
B	Numerical Simulations Code	64
B.1	OpticalOneLayer.m	64
B.2	OpticalFourLayer.m	68
B.3	OpticalSphere.m	73
B.4	Magnetic2d.m	76
B.5	Magnetic3d.m	80

List of Figures

1.1	Solutions of colloidal silver, nanocrescents and colloidal gold. [1] . . .	8
1.2	A TEM image of a gold nanocrescent. [1]	11
2.1	The complex dielectric functions of gold and silver	17
2.2	Extinction spectra for 10 nm diameter gold spheres in various media using the electrostatic approximation.	22
2.3	Calculated scattering and absorption spectra for 20 nm diameter gold spheres in various media using Mie theory in spherical coordinates.	27
2.4	Calculated absorption spectra for gold cylinders of various diameters in air of using Mie theory in cylindrical coordinates.	29
3.1	The dipolar and quadripolar field profiles of the 200 nm outside diameter gold nanocrescent in air.	36
3.2	Local Field Enhancement spectra for a 200 nm outside diameter gold nanocrescent in various media.	37
3.3	Local Field Enhancement spectra for 200 nm and 300 nm outside diameter gold nanocrescents in gelatine.	38
3.4	Local field enhancement spectra for 300 nm outside diameter gold and silver nanocrescents in gelatine.	40
3.5	The four layer gold, iron, silver, gold nanocrescent and gold nanonanosphere with incident light from the left.	41
3.6	Graphical representation of the nanocrescent alignment for maximum torque, which is on the order of 10^{-19} N-m for the four-layer nanocrescent studied.	46
4.1	A summary of the experimental setup used in our spectral imaging system.	48
4.2	A true color image of the nanoparticle sample region analyzed.	49
4.3	A scanning electron microscope (SEM) and true color image of the nanowires analyzed.	50

4.4	Experimental scattering spectra from the gold nanoparticle solution. .	51
4.5	Experimental scattering spectra for 60, 80 and 120 nm wide gold nanowires.	52

Chapter 1

Introduction

1.1 What are Nanoplasmonic Probes?

Biocompatible nanoplasmonic probes are metallic nanostructures that can be used for *in vivo* cellular imaging and high throughput applications including biomolecular identification, screening and biochemical reaction characterization. Specific applications include detecting and imaging single protein molecules, monitoring cellular enzymatic activity via Surface Enhanced Raman Scattering (SERS) and *in vivo* surface plasmon resonance (SPR) spectroscopy sensors for optically quantifying biomolecular reactions in real-time.

Their utility depends upon the unique physical phenomena that manifest themselves on the nanometer scale. In particular, surface plasmon resonance dominates the spectral characteristics of probes on this size scale, resulting in narrow extinction peaks and large local electromagnetic field enhancements. The resonant frequency of metallic nanoparticles depends strongly upon the dielectric properties of the local medium and changes can be quickly and accurately detected optically, providing great temporal and spatial sensitivity and specificity. The plasmon resonance can be shifted into the near infrared (NIR) spectrum specifically for *in vivo* applications through careful engineering so that the excitation light is not attenuated or scattered by water and can penetrate living tissue effectively.

Localized surface plasmon polaritons as found in metallic nanoparticles will be our primary interest in this paper for their applications in biocompatible nanoplasmonic probes with potential *in vivo* applications, however propagating modes will also be considered and their applications will be noted. A plasmon is a quantized charge density wave, which is manifested classically as a propagating longitudinal wave of charge carriers, typically electrons in the solid state. Plasmons exist in con-

ducting media, such as metals, semiconductors and plasmas, both in the bulk and on the surface. At the surface, plasmons interact strongly with electromagnetic waves resulting in a coupled, localized optical-electrical elementary excitation known as a surface plasmon polariton, which may propagate at the interface of two media when certain constraints are met. A polariton is a quantum mechanical phenomenon in which a photon is coupled with another excitation, such as a plasmon or phonon. The term surface plasmon is an informal term for a surface plasmon polariton and both terms will be used throughout this paper.

Localized surface plasmon-polariton modes manifest themselves as polarization modes and result in significant local electric, magnetic and polarization field enhancements. At plasmon resonance, the effective scattering and absorption cross sections of nanoparticles are significantly larger than their geometrical cross section, which vastly improves the sensitivity of nanoplasmonic probes as compared to other cellular probes for detection applications. They can be interpreted both quantum mechanically and classically and both types of language will be used when appropriate. Mie theory provides the firm theoretical background to describe the absorption properties, internal fields and scattered far fields of dielectric particles.

Chapter 1 will introduce nanoplasmonic probes to the reader and discuss their properties and applications in qualitative detail. Chapter 2 will discuss the relevant theory with an emphasis on applications and computationally solve the equations that correspond to well characterized physical situations. Chapter 3 will review the numerical simulations performed to characterize nanoplasmonic probes and discuss their relevance as a rapid design and testing platform for nanoplasmonic probes. Chapter 4 will review the results of an experiment designed to demonstrate a new technique for the high throughput, label-free identification of biomolecules and characterization of biochemical processes using nanoplasmonic probes. Chapter 5 will discuss future research goals.

1.2 A Survey of Nanoplasmonic Probes

1.2.1 Colloidal Metal Nanoparticles

Colloidal metal nanoparticles from 5 - 150 nm in diameter can be chemically synthesized cheaply and easily and are the most historic of the nanoplasmonic probes surveyed in this chapter. Metallic nanoparticles are also commonly referred to as metal clusters, however the former notation will be used throughout this paper. Gold nanoparticles have been used for centuries in stained glass windows for their bright red coloring due to the selective absorption of incident light due to SPR. Gustav Mie



Figure 1.1: Solutions of colloidal silver, nanocrescents and colloidal gold. [1]

developed his landmark electromagnetic theory in 1908 primarily to quantitatively describe the optical properties of colloidal gold. The dominant surface plasmon polariton modes of gold, silver, copper and platinum nanoparticles can be engineered to fall in the visible spectrum. A number of nanoplasmonic probes in solution illuminated by a white light source are shown in Figure 1.1. From left to right, the solutions contain 40 nm colloidal silver, 80 nm colloidal silver, gold nanocrescents, 50 nm colloidal gold, and 5 nm colloidal gold. The solution colors depend upon the scattering and absorption spectra of the nanoplasmonic probes they contain, which depend upon a number of parameters including size. It will be proven later that both localized and propagating surface plasmon-polariton modes only exist at the interfaces where a positive dielectric function and negative dielectric function material meet, with the dielectric functions assumed to be purely real.

Although the resonant behavior of individual, well separated metallic nanoparticles is strong and controllable, they tend to aggregate into large groups that can precipitate out of solution, and in which interparticle interactions involving the near-field electric fields and the longer dipolar fields can lead to unpredictable results. Single scattering hot sites with very large local field enhancements have been reported in metallic nanoparticle aggregates with local field enhancements up to 10^{14} [2]. However, techniques for the accurate engineering of such sites have not been developed. Individual metallic nanoparticles exhibit a significant local field enhancement at SPR, but the resonant frequency can not be shifted into the NIR due to their simple geometry, which reduces their applications as *in vivo* SERS substrates

and biosensors except in aggregate form.

A technique for controllably aggregating silver colloids should be mentioned because it has been used to probe various biomolecules, including proteins, enzymes and the mutations of the regulator gene for cystic fibrosis [3] [4] [5]. By reducing the silver colloid in such a way that a negatively charged citrate surface layer is formed, the nanoparticles will not aggregate and will remain in solution. Aggregates of controlled size can be formed by introducing cations or acids into the solution to modify the pH. In this manner, the single hot sites that randomly appear in large aggregates are spread throughout the aggregate due to the formation of small, orderly clusters which remain in solution and exhibit Brownian motion.

Gold is the most prevalent material used in the biological sciences because it does not readily oxidize like silver and its surface can easily be conjugated using peptides and antibody groups. Such functionalized, high specificity probes can be used to selectively target specific biomolecules and tissues *in vivo*. Metallic nanoparticles, especially gold, are useful as nanoplasmonic probes and they exhibit a strong plasmonic response at sites in clusters that experience a significant interparticle mode coupling. However the lack of reproducibility of such effects and a general lack of actual and control mechanisms has led research groups to develop other probe designs.

1.2.2 Gold Nanoshell

Although metallic nanoparticles exhibit a large plasmon response and local field enhancement, especially in aggregates when there is a significant amount of interparticle coupling, their plasmon response can not be engineered over a very wide spectrum. The engineering and design capabilities of the single nanoparticle were vastly improved by modifying its geometry to that of a thin metal shell surrounding a spherical dielectric core. The SPR frequency of the metal nanoshell is determined by the degree of surface mode coupling between the inner and outer metallic surfaces, or equivalently, by the ratio of shell thickness to the mean shell radius. The final resonance frequencies of the gold nanoshell exist as hybrid modes generated from the inner and outer plasmon resonances and the hybridized theory has many analogies to molecular orbit theory [6]. The optical resonance can be engineered to lie anywhere in the visible spectrum and well into the NIR [7]. The overall scattering and absorption behavior of nanoshells is determined by their size; particles much larger than the quasistatic limit primarily scatter light whereas smaller particles absorb it.

The dipole limit of a nanoparticle is reached when its size is much smaller than the wavelength of light and the electric field can be approximated as constant across it. Nanoshells with smooth surfaces in the dipole limit approach the behavior of

single metallic nanoparticles due to the dominance of the dipolar excitation mode, which will be explained in Chapter 2. Silver nanoshells display plasmon frequencies that are blue shifted and more intense compared to gold nanoshells of similar sizes [8].

The absorption cross-section of the gold nanoshell, and other nanoplasmonic probes, is approximately six orders of magnitude greater than comparable, conventional NIR fluorescent dyes such as indocyanine green [9]. The plasmon response of a hollow metal nanoshell can be analyzed as the interaction between the surface plasmon polariton modes on the outer surface and on the inner surface of the shell through near-field electromagnetic field coupling. Rather than the single plasmon resonance displayed by metallic nanoparticles, nanoshells exhibit two resonance peaks corresponding to the symmetric and antisymmetric surface eigenmodes.

The dielectric properties of the dielectric core and surrounding medium affect the plasmon response, and the response rate of the optimized gold nanoshell varies between 100 and 200 $\frac{nm}{RIU}$ (Refractive Index Unit), which is comparable to the response of solid nanoparticles [10]. The spectral width of the gold nanoshell is relatively wide, with reported values of 760 meV (1632 nm) for a group of nanoshells suspended in solution and 540 meV (2298 nm) for an individual nanoshell attached to the surface of a conductive substrate [11]. The spectral width of the plasmon peaks is wider than other nanoplasmonic sensors and the primary benefit of nanoshells over nanoparticles is the ability to engineer the response of the former.

Gold nanoshells are produced via molecular self-assembly and reduction reactions which can be scaled to produce large quantities cheaply. The nanoshell production method is a prototypical example of the bottom up approach to nanotechnology, which emphasizes self-assembly and chemical reactions whereas top down approaches emphasize semiconductor manufacturing techniques such as electron gun and chemical vapor deposition, thermal oxidation and lithography. To produce gold nanoshells, monodisperse silica nanoparticles are grown via the Stöber method [12], through which alkyl silicates are hydrolyzed into silicic acid in an alcohol solution to generate the nanoshell dielectric core. Next, 3-Aminopropyltriethoxysilane is adsorbed onto the surface of the silica nanoparticle in an aqueous solution resulting in the growth of an amine surface layer. Then, nanometer sized gold colloids are introduced to the solution which readily bond to the amine ligands with approximately 30% coverage. Finally, a mixture of chloroauric acid and potassium carbonate is reduced by sodium borohydride to grow a uniform gold shell from the gold colloid seeds. The basic silica-amine-gold colloid is modular and effective enough to be applied to other transition metal nanoshells such as silver. As would be expected, gold nanoshells are much less thermodynamically stable than their bulk material counter-

parts. The deposition of an additional 60 nm silica thin film to seal the gold nanoshell results in its effective melting temperature increasing from 325 °C to 600 °C without any measurable effect on its optical properties.

Gold nanoshells are useful in cellular imaging because their tuned frequencies can be used for single light source multiplexing and their surfaces can be conjugated with antibodies or peptides to attach to specific cell and protein binding sites [13]. Additionally, at SPR they are very efficient at converting the excitation light energy into thermal energy, which can be used for the localized thermal ablation of selected tissues such as cancerous tumors *in vivo* using a NIR excitation light source. Although gold nanoshells exhibit a significant local field enhancement at resonance, reportedly on the order of 10^2 [14], other nanoplasmonic probes such as the nanoring and nanocrescent have been developed specifically as SERS substrates that maximize the local field enhancement [15].

1.2.3 Nanocrescent

The nanocrescent is a recent nanoplasmonic probe design that is being developed at UC Berkeley in the BioPOETS (Biomolecular Polymer OptoElectronic Technology and Science) group in the Bioengineering department under Professor Luke Lee [1]. It improves upon past probe designs by including sharp tips which increase intraparticle mode coupling between the cavity and outside surface modes and strong tip-tip interactions leading to a significant local electromagnetic field enhancement at the tips and additional degrees of freedom for optimization. A transmission electron microscopy (TEM) image of a gold nanocrescent cross-section can be seen in figure 1.2.

The intraparticle mode coupling interactions dominate the electromagnetic properties of the nanocrescent and small changes in terms of the opening aperture diameter, inside and outside diameters can significantly change its optical properties. The plasmon frequency of nanoparticles and the nanoshell can be tuned by embedding them into high refractive-index substrates. However, additional complexity and reduced symmetry of the nanocrescent with respect to the nanoshell increases the degrees of freedom available to tuning. Biomolecules can be adsorbed at the tip aperture for increased spatial resolution and greater local field enhancement than other nanoplasmonic probes.

The gold nanocrescent is fabricated using a top down approach by rotationally evaporating a thin gold layer using electron beam deposition onto a sacrificial polystyrene nanosphere at an angle. The coated nanospheres are then released into aqueous suspension by acetone, collected and the sacrificial nanospheres are sub-

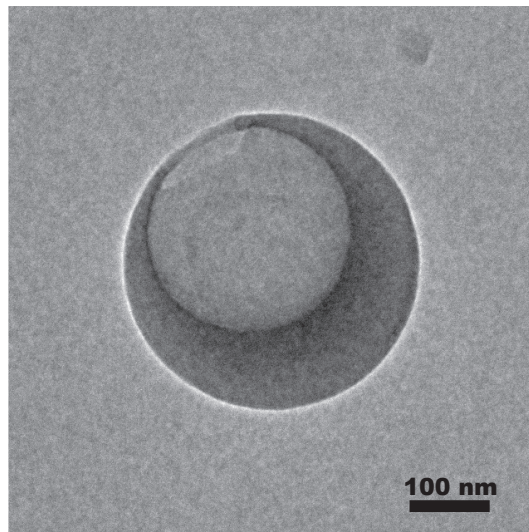


Figure 1.2: A TEM image of a gold nanocrescent. [1]

sequently dissolved using toluene. There are both benefits and drawbacks to the nanocrescent fabrication process compared to colloidal metals and nanoshells. It is relatively expensive, in that the required vacuum chamber and deposition equipment both require a significant amount of capital and the overall processes does not scale as well as self-assembly fabrication techniques. However, the deposition process can be adapted to any material that can be sputtered or electron beam deposited, such as iron for magnetically modulated nanocrescents, which will be discussed later. Additionally, the geometry of the nanocrescent can be well controlled by changing the deposition angle and sacrificial nanosphere size and future nanoplasmonic probes will be able to utilize similar equipment if they are designed appropriately.

1.2.4 Semiconductor Quantum Dots

Quantum dots are semiconductor nanocrystals that have unique electronic bandgap properties, which translate into useful optical properties for bioengineering and applied physics applications such as single electron transistors [16]. They are typically binary compounds from groups II and VI or II and V, with common examples being CdSe, CdS, ZnSe, ZnS, InP and InAs. While quantum dots *are not* nanoplasmonic probes, there are still of interest and can be considered a closely related technology

in all of the applications that nanoplasmonic probes are used for, except SERS.

The useful optical properties of metal nanoparticles are derived from the rapid increase in absorption and scattering at plasmon resonance, while the properties of quantum dots are derived from a specific, controllable emission energy due to the quantum mechanical confinement of excitons generated from incident photons. The exciton wave function and energy eigenvalues can be approximated using the classic introductory quantum mechanical problem of the free-particle in the three dimensional energy well, where the boundary conditions lead to discrete permissible system states. As the size of the well or quantum dot increases, the energy eigenvalues decrease and emission photons move to longer wavelengths. For example, a 3 nm diameter CdSe quantum dot will emit at 520 nm while a 5.5 nm CdSe will emit at 630 nm [17].

Quantum dots can be excited in a broad spectrum band above the particular characteristic emission wavelength and they find biological applications in cellular imaging, multiplexed tagging and optical identification. Organic fluorophores, which have been the dominant technological approach to cellular imaging and tagging over the past several decades, have an asymmetric, narrow, absorption band that is at a slightly higher energy than the emission band. Therefore each fluorophore can only be excited at a specific wavelength using specific light source. Commonly encountered organic fluorophores include fluorescein and Rhodamine 6G, which have been used in real-time imaging of live cells, gene expression profiling cell sorting and clinical diagnostics.

Several problems with quantum dots which have been solved in the past few years include cytotoxicity concerns, hydrophobicity, and blueshifting. By encapsulating quantum dots in micelles, phospholipid membranes, they can simultaneously be made hydrophilic and biocompatible, although they are still fragile. Quantum dots have been used to image the tissue of living frogs [17] and they can be conjugated using peptides and single strands of DNA to provide biomolecular binding specificity. The quantum yield, or the average ratio of the emitted photons to the number absorbed, can reduce over time due to photoinduced crystal defects. It can be improved by capping quantum dots with higher bandgap energy shells which remove the electronic excitation from the surface in contact with the environment. The quantum yield can be improved by reducing the number of surface trapping states and crystal defects that can prevent the recombination of the exciton pair and subsequent photon emission. Additionally, oxidizing environments and photoinduced oxidation can decrease the core quantum dot size and blueshift the emission wavelength.

1.3 Applications of Nanoplasmonic Probes

1.3.1 Surface Enhanced Raman Spectroscopy

Raman scattering, the inelastic scattering of light from matter, was discovered in 1928 by Chandrasekhara Raman, who received the Nobel prize in 1930 for his discovery [18]. Modern Raman spectroscopy is a robust, label-free technique that requires very little sample preparation and is used to study the low-frequency vibrational and rotational energy levels of single molecules via Raman scattering. The Raman spectroscopy signature of a molecule is like a fingerprint and can be used for both characterization and rapid identification once a signature is known and stored in a database. The light is inelastically scattered due to the absorption of energy by phonons and other excitation modes. By illuminating a sample with a monochromatic laser beam and then sending the scattered light through a monochromator and spectrometer, the incident wavelength can be filtered out and the Stokes and anti-Stokes shifted light, corresponding to a decrease and increase in energy respectively, can be detected and analyzed. Enzymatic activity can be detected by studying the changes in the chemical bonds in molecules when specific proteins are added. Raman spectroscopy can be used in gas, liquid and condensed matter research. Actual spatial and temporal resolutions vary significantly between laboratory tools and particular arrangements, however there are many reports of single molecule detection and protein studies using SERS [19] [20] [21]. Raman spectroscopy has recently demonstrated in the *ex vivo* characterization of breast tissue [22]. The non-invasive optical detection of breast cancer carries a number of benefits, including reduced cost due to automation, reproducibility, portability and a vastly reduced turn-around time from several months to several minutes.

Surface Enhanced Raman Scattering (SERS) was discovered experimentally in 1974 from experiments using pyridine adsorbed onto a roughened silver electrode surface [23]. There are two mechanisms that contribute to SERS; an electromagnetic one and a chemical one [24]. The electromagnetic contribution is the less complicated mechanism and results in the rate of Raman scattering, which is usually exceptionally low, scaling according to E^4 [25]. The maximum local field enhancement in nanoplasmonic probes on resonance can be on the order of E^8 , and the overall SERS effect transforms a very weak, anomalous effect into a useful, non-destructive, highly informative spectroscopic technique.

1.3.2 Proteomics

Nanoplasmonics has been actively contributing to the field of proteomics for years, successfully identifying and characterizing single protein molecules and monitoring enzymatic activity *in vivo* using silver colloids [3] [5]. Proteomics is the next logical step in the reductionist approach to molecular cellular biology [26]. Gene and protein expression are the processes by which the information stored in nucleic and amino acids is converted into proteins and cellular structures and functions. Proteomics relies upon our ability to identify proteins in order to quantify the expression of specific genes, measure protein diversity and to isolate and replicate specific proteins for more detailed study using techniques like x-ray crystallography.

High sensitivity, high throughput microassays were developed in the late 1950s to measure the concentrations of hard to detect biomolecules such as hormones [27]. Assays are the interface through which nanoplasmonic probes and other sensors and markers discussed in this paper interact with the desired biomolecules. Microassays include ligand assays such as immunoassays, which utilize antibody-antigen bonding for specificity, and polynucleotide assays, which utilize single stranded DNA bonding.

Microassays are of interest because the measurement volume and times are greatly reduced while sensitivity is greatly increased. Sensitivity can be expressed in quantitative terms as the ratio of response rate of measured signal to input, commonly referred to as the dose-response rate [27]. By using smaller sensors, the measured variable is disturbed less by the act of measurement. For example, introducing a large thermometer into a very small volume of water will change the measured temperature to such a large extent to the heat capacity of the thermometer that the significance of the data becomes negligible. Similarly, the sensitivity of small sensor volumes is counter intuitively greater than macroassays.

Biosensors, such as nanoplasmonic probes, act as the signal mediator to yield quantitative measurements of binding event frequencies and timing with both temporal and spatial sensitivity between the analyte of interest and the label or assay. Assays can be designed to either measure the number of binding sites (noncompetitive) or to measure the difference between the number of unbound sites before and after the reaction (competitive), although the former approach has been proven to be more accurate in practice [27]. Multiple binding agents can be used to increase sensitivity and statistical significance. Typical labels include radioisotopes, enzymes, fluorophors and chemiluminescent markers that signal binding reactions through measurable pathways, such as by the production of photons. The sensitivity of a binding assay can be interpreted as the total measurable signal produced per analyte molecule in solution, and sensitivity can be increased by using assays with higher binding affinities and sensors with higher quantum yields and spectrally

narrow emission spectra, for example.

High throughput protein identification systems are currently primarily based upon mass spectrometry and two dimensional gel electrophoresis. Both techniques depend upon cleaving proteins and separating them by mass and charge, and both will continue to be useful for performing laboratory studies of molecular structure. However, there are several reasons that optical identification techniques will provide better high throughput results in the future. First, proteins can be selectively tagged with optically active markers such as nanoplasmonic probes or quantum dots by peptide or antibody conjugation, and a single light source can be used to excite multiple markers at once. Furthermore, single protein molecules can be studied using label-free techniques such as SERS and SERRS immunoassays [3]. Both Raman spectroscopy and other optical identification techniques are non-destructive and label-free techniques that can be utilized to minimize the chance of any conformational changes or the possibility of denaturing during *in vivo* detection. Protein expression varies widely within cells and tissue and nanoplasmonic probes can be used to track and characterize proteins over time and *in vivo*. Finally, nanoplasmonic probe assays can be miniaturized, arrayed and integrated into protein biochips with the potential to change proteomics in the way that DNA biochips have revolutionized genomics and lead to the completion of the Human Genome Project.

Most of the issues that are making it difficult to development a human proteome database in analogy to the successful human genome project are related to a lack of sensitivity and statistical certainty. Approximately 90% of all protein matter in living human tissue is composed of just 10% of the estimated human proteome database, which means that proteomics is essentially the study and characterization of background noise in terms of concentrations. Even in simplest known living organism, *Mycoplasma genitalium*, only 73% of the total estimated proteins have been observed and 32% have been characterized in detail [27]. The polymerase chain reaction (PCR) that is widely used to duplicate small sections of DNA for characterization does not have a protein equivalent and the development of highly sensitive analytical techniques is required for future breakthroughs in proteomics.

Chapter 2

Theory

Small particles on the order of the wavelength of light exhibit a number of novel optical properties and can be both very efficient scatterers and absorbers of electromagnetic waves [28]. The first mathematically rigorous theory for the scattering of an incident plane wave on an isotropic, non-magnetic, optically linear dielectric sphere of any size in a homogenous, non-absorbing media was developed in 1908 by Gustav Mie, with notable earlier independent contributions from Alfred Clebsch and Ludvig Lorenz [29]. Mie theory encompasses the more commonly encountered Rayleigh scattering theory at very small sizes and is the more general theory.

The scattered fields as described by Mie theory are applicable to all classes of solid matter, however electromagnetic surface modes that are negligible in insulators become noticeable in many crystal lattices and pronounced in metals, resulting in a number of excitation eigenmodes at which the scattering and absorption of incident light is vastly increased. Both surface phonon-polaritons and plasmon-polaritons exist in solid state matter, however we will only discuss the theory behind latter. Charge carriers, such as the valence electrons that are always present in a metal or the quantized lattice waves in all crystals, commonly known as phonons, are required for the appearance of localized surface modes to satisfy Maxwell's equations where $\nabla \cdot \mathbf{E} \neq 0$.

The terms surface plasmon, surface plasmon resonance and surface plasmon polariton are used interchangeably in literature to describe both the propagating modes found in thin films (see section 2.6) and the localized surface modes found in metallic nanoparticles. The electromagnetic character of the two plasmon polariton modes varies significantly and great care must be taken not to confuse their respective governing equations and results. For example, localized surface plasmon polariton modes result in the increased scattering of light, whereas in thin films they result in

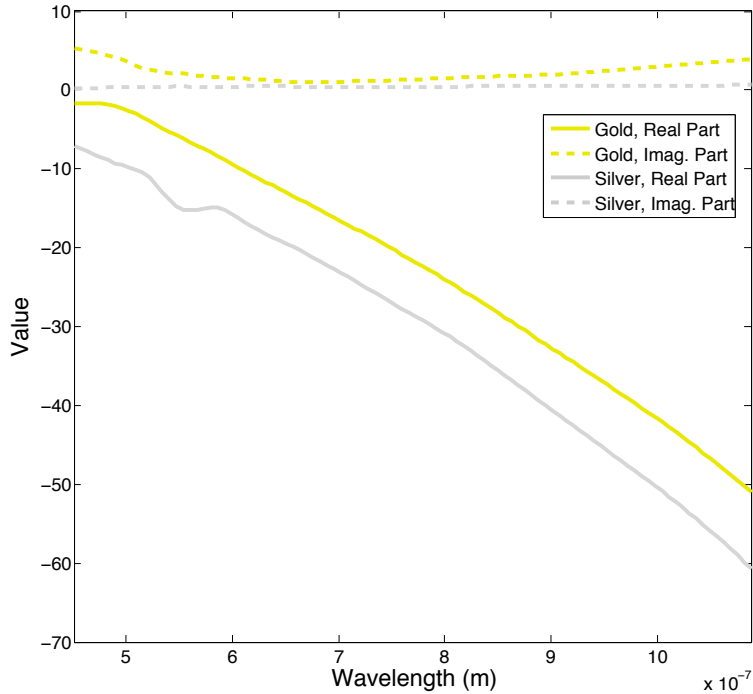


Figure 2.1: The complex dielectric functions of gold and silver based upon experimental data [31].

the complete absorption of polarized light.

Bulk propagating longitudinal electron waves, or plasmons, only appear in metals at the plasma frequency when $\epsilon(\omega) = 0$. Propagating surface plasmon-polaritons and surface plasmon-polariton normal modes, distinguishable from bulk plasmons that occur away from the surface, can occur at any frequency when $\epsilon(\omega) < 0$ and wave vector components tangential to the surface are matched. In quantum mechanical terms, the momentum of the incident photon and the generated plasmon-polariton must be matched, which can occur in thin metal films at the boundary of a dispersive medium and in diffraction gratings [30].

The localized electromagnetic surface modes can appear due to both phonon-polaritons and plasmon-polaritons in nanoparticles. However, in this case the dominant feature is the surface electromagnetic field and the induced polarization rather than a propagating wave at the boundary. The momentum matching condition does not apply in the case of localized surface modes, which increases their range

of feasible applications significantly. Coupling between bulk plasmons and surface plasmon-polaritons is typically negligible for the particle sizes and optical frequencies that are of practical interest [32].

SPR theory is awkward to describe without the extensive use of mathematical symbols, particularly due to the prevalence of complex numbers. The dielectric function, as well as other functions and variations, will be often be referred to in the form $y = y' + iy''$, where the single prime denotes the real part and the double prime denotes the imaginary part of the variable or function. Additionally, the interface of a dielectric medium and a metal will often be considered, and the properties of the media will be referred to in the form y_i and y_o , where the former refers to the metal properties and the latter refers to the outside dielectric medium.

Nanoplasmonic probes can be engineered for a number of different applications, and the design goals and constraints can vary widely. Thermal ablation and SERS probes for biomolecular detection are engineered to have a very high absorption cross-section for localized heating or local field enhancement and a resonance peak in the NIR for *in vivo* compatibility. Cellular imaging probes and probes designed for high throughput spectral imaging require narrow, controllable and well characterized scattering peaks with negligible absorption. These design goals can be achieved through the theory of this chapter and verified through numerical simulations and experiments, which will be discussed in Chapters 2, 3 and 4.

2.1 The Complex Dielectric Function

The complete response of crystalline materials to electromagnetic waves is encapsulated by the frequency dependent dielectric function. It will be proven later in this chapter that the most general electromagnetic requirement for the excitation of surface plasmon-polaritons, which applies to both thin films and nanoplasmonic probes, is that $\epsilon'_i < 0$ and $\epsilon'_o > 0$. Most solid state dielectrics have positive values of ϵ' and they are commonly encountered in all fields of science. Most metals have a negative value of ϵ' below the plasma frequency, which can be interpreted as the maximum oscillation frequency at which the electrons in the metal.

The Drude model of metals supplies the real part of the complex dielectric function at visible and ultraviolet frequencies as [28]

$$\epsilon'(\omega) = 1 - \frac{\omega_p^2}{\omega^2} \quad (2.1)$$

where ω_p , the plasma frequency, is given by

$$\omega_p^2 = \frac{Ne^2}{m_e \epsilon_0} \quad (2.2)$$

where N , e and m_e are the electron density, charge and mass, respectively. (2.1) is useful as a first order approximation, however it assumes that the dielectric function depends solely upon frequency and does not account for wave dispersion effects or electron transitions.

The plasma frequency is the critical value below which ϵ' is negative. At frequencies below it, the electrons in the metal oscillate in phase with the incident field and rapidly attenuate the field in the direction of propagation. Thus, propagating transverse waves are not supported below the plasma frequency, as can be verified by the fact that metals are opaque and can reflect light at optical frequencies.

Above the plasma frequency, metals are essentially transparent and absorption is negligible. As the frequency approaches ω_p , ϵ' approaches zero from the negative side and ϵ'' approaches zero from the positive side. It can be shown that at ω_p , bulk plasmons are valid solutions to Maxwell's equations and can be observed experimentally as longitudinal charge waves where $\nabla \cdot \mathbf{E} \neq 0$. For most metals the plasma frequency lies in the ultraviolet and light x-ray range, however for noble metals such as gold, silver and copper it lies in the near ultraviolet and visible spectrum, which is the source of their distinctive colors.

The optical properties of a wide range of metals are summarized in table 2.1. It will be shown that the value of ϵ'' at plasmon resonance is directly proportional to the width of the scattering and absorption resonance peaks. For applications that require a narrow resonance peak, the optical properties of silver are better suited than gold due to its much lower value of ϵ'' . However, there are three reasons that gold is often better suited for bionanophotonics applications. First, silver readily oxidizes in most environments unless special care is taken and the formation of a surface oxide layer disrupts its nanoplasmonic properties. Second, the plasmon resonance of gold is inherently at a longer wavelength than silver due to the more negative ϵ' of the latter (Fig. 2.1). The plasmon resonance frequency of nanoplasmonic probes can be engineered using structures like the nanoshell and nanocrescent, so the issue of resonance wavelength is not absolute. Finally, gold surfaces are more often terminated by ligands or peptides with high binding specificity in literature than silver and presumably the techniques used for gold are better characterized.

Selected equations in this chapter were solved and plotted in MATLAB. All figures are original and can be generated by running the source code included in the Appendix. One aspect of Mie scattering that will not be discussed in this chapter is the angular dependence of the scattered intensity. That topic is beyond the scope of

Table 2.1: Properties of Bulk and Surface Plasmons in Selected Materials [28]

Solid	Bulk Plasmon Energy (eV)	Surface Plasmon Energy (eV)	ϵ'' where $\epsilon' = -2$
Lithium	6.6	3.4	1.0
Sodium	5.4	3.3	0.12
Potassium	3.8	2.4	0.13
Magnesium	10.7	6.3	0.5
Aluminum	15.1	8.8	0.2
Iron	10.3	5.0	5.1
Copper	—	3.5	4.9
Silver	3.8	3.5	0.28
Gold	—	2.5	5.0
Graphite	—	5.5	2.7

this paper and the reader is referred to other, more advanced resources [28] [33].

2.2 Surface Modes in Spheres, The Electrostatic Approximation

In the case of spherical particles much smaller than the incident wavelength, the phase δ of the electromagnetic field across the particle is negligible and a complex scattering and absorption problem is reduced to a set of electrostatic equations. The dielectric functions of metal clusters larger than the electron mean free path, on the order of 10 nm, are identical to their bulk counterparts and are size independent. Clusters that are on the order of several nanometers in diameter have size-dependent dielectric functions which must be accounted for to yield accurate results. We will primarily be concerned with clusters between 10 and 30 nm in diameter in this section. An extensive and interesting discussion of the size dependent dielectric function can be found in Kreibig [33].

The electrostatic approximation assumes that the electric field is spatially constant across the sphere and the magnetic field is negligible, although the former field

still has a sinusoidal time dependence, and that there are no free charges. These assumptions lead to the following Maxwell's equations in differential form.

$$\begin{aligned}\nabla \cdot \mathbf{D} &= 0 \\ \nabla \times \mathbf{E} &= 0.\end{aligned}\tag{2.3}$$

By expressing both equations in terms of the polarization field, P , the following two equations are obtained.

$$\frac{\epsilon_i(\omega)}{\epsilon_i(\omega) - 1} \nabla \cdot \mathbf{P} = 0\tag{2.4}$$

$$\frac{1}{\epsilon_i(\omega) - 1} \nabla \times \mathbf{P} = 0\tag{2.5}$$

where ϵ_i is the frequency dependent complex dielectric function of the particle. There are three possible solutions:

1. $\nabla \cdot \mathbf{P} = 0$ and $\epsilon_i(\omega) = \infty$, which corresponds to propagating transverse modes in the sphere. These are not supported by metals when $\epsilon < 0$.
2. $\nabla \times \mathbf{P} = 0$ and $\epsilon_i(\omega) = 0$, which corresponds to bulk longitudinal plasmon modes.
3. $\nabla \cdot \mathbf{P} = 0$ and $\nabla \times \mathbf{P} = 0$, which corresponds to the surface plasmon-polaritons, which can be polarization normal modes in metal spheres in the electrostatic approximation.

The electromagnetic fields from the third solution can be solved for and the resonant frequencies are found by the following characteristic equation

$$\epsilon_i(\omega_l) = \epsilon_o \frac{l+1}{l}, \quad l = 1, 2, 3, \dots\tag{2.6}$$

where ω_l is the frequency of the l th surface mode. The surface mode frequencies and polarization modes will be solved in detail in the following sections. As noted earlier, higher order modes in the electrostatic approximation (when $l > 1$) are negligible so when $\epsilon_i(\omega) = -2\epsilon_o$, the polarization field is typically at a resonance maximum. The dipolar mode is also commonly referred to as the Fröhlich mode in

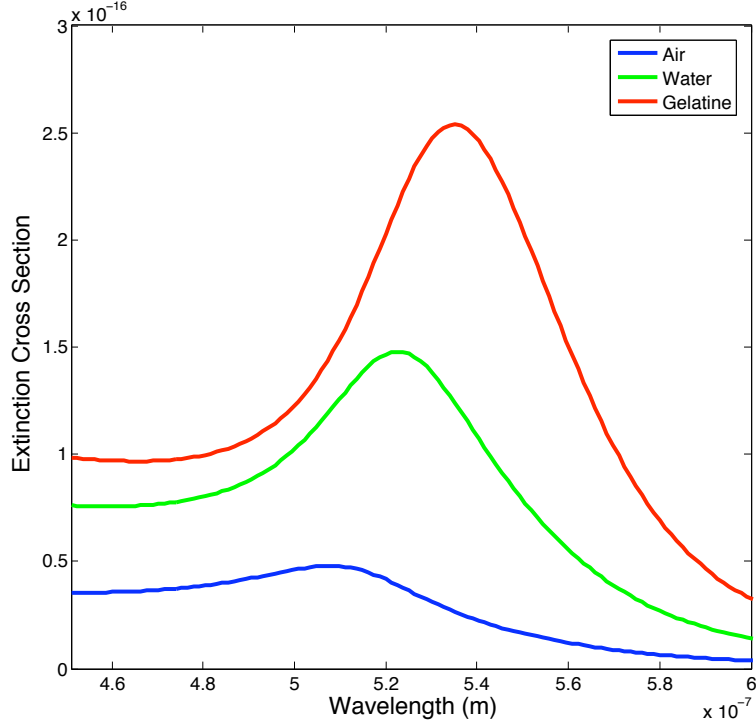


Figure 2.2: Extinction spectra for 10 nm diameter gold spheres in various media using the electrostatic approximation.

literature. The electric fields inside and outside the sphere are described by spherical harmonics of order l .

In the electrostatic limit, scattering is dominated by absorption [33]. The total extinction cross section written in explicit complex variable notation is

$$\sigma_e(\omega) = \frac{54\pi^2}{\lambda} \frac{\epsilon_o^{3/2} R^3 \epsilon_i''(\omega)}{[\epsilon_i'(\omega) + 2\epsilon_o]^2 + (\epsilon_i'')^2} \quad (2.7)$$

The plasmon resonance width, is [33]

$$\tau \propto \frac{2\epsilon_i''}{\sqrt{\left(\frac{\partial \epsilon_i'}{\partial \omega}\right)^2 + \left(\frac{\partial \epsilon_i''}{\partial \omega}\right)^2}} \quad (2.8)$$

(2.7) and (2.8) imply that the plasmon resonance frequency is determined by both

ϵ'_i and ϵ''_i and that the resonance width is smallest for materials with small ϵ''_i and rapidly changing dielectric functions. The four metals that have optical dielectric functions when immersed in low refractive index media are gold, silver, copper and aluminum (Table 2.1).

It is important to note, particularly in the design of nanoplasmonic probes, that the surface mode frequencies depend heavily upon the dielectric function of the embedding medium. An increased dielectric function is indicative of a more easily polarized material and as the dielectric function of the embedding material increases the restoring force on the electrons decreases. The motion of the surface electrons is analogous to a damped, sinusoidally driven spring system. The final frequency of the system is a function of the natural frequency of the electrons, the damping forces present and the driving frequency, and as the damping force increases the actual frequency decreases resulting in a red-shift and damping of the plasmon resonance modes. By sensing the shift in the plasmon resonance frequency the dielectric function of the local environment can be calculated and functionalized, optically sensed bioassays are being developed based upon this principle, and this type of sensor is generically called an SPR spectroscopy biosensor.

The extinction spectra of 10 nm diameter gold spheres in various media calculated using the electrostatic approximation are shown in figure 2.2. The dielectric functions of the immersing media are approximated as completely real and frequency invariant. The dielectric functions of air, water and gelatine used are 1.0, 1.79 and 2.37, respectively. The strong dependency of the resonance frequency, intensity and width on the outside dielectric function is shown.

2.3 Formulation of the Helmholtz Equation

Maxwell's equations in polarizable, conducting, homogenous and isotropic media can be written in the following form [28]

$$\begin{aligned}\nabla \cdot \mathbf{D} &= \rho \\ \nabla \cdot \mathbf{B} &= 0 \\ \nabla \times \mathbf{E} &= -\frac{\partial \mathbf{B}}{\partial t} \\ \nabla \times \mathbf{H} &= \mathbf{J} + \frac{\partial \mathbf{D}}{\partial t}\end{aligned}$$

where \mathbf{E} is the electric field, \mathbf{D} the electric displacement, \mathbf{H} the magnetic field and \mathbf{B} the magnetic induction. \mathbf{D} and \mathbf{H} are defined as

$$\begin{aligned}\mathbf{D} &= \epsilon_0 \mathbf{E} + \mathbf{P} \\ \mathbf{H} &= \frac{\mathbf{B}}{\mu_0} - \mathbf{M}\end{aligned}$$

where \mathbf{P} is the electric polarization, \mathbf{M} the magnetization, ϵ_0 the permittivity of free space and μ_0 the permeability of free space. The following constitutive relations complete our set and allow us to form the field equations when subjected to harmonic fields.

$$\begin{aligned}\mathbf{J} &= \sigma \mathbf{E} \\ \mathbf{B} &= \mu \mathbf{H} \\ \mathbf{P} &= \epsilon_0 \chi \mathbf{E}\end{aligned}$$

Where σ is the electrical conductivity, μ the magnetic permeability and χ the electric susceptibility.

When such media are subjected to a time varying harmonic field with an assumed $e^{-i\omega t}$ time dependence, these equations result in the following complex field equations

$$\nabla \cdot (\epsilon \mathbf{E}) = 0 \quad (2.9)$$

$$\nabla \cdot \mathbf{H} = 0 \quad (2.10)$$

$$\nabla \times \mathbf{E} = i\omega \mu \mathbf{H} \quad (2.11)$$

$$\nabla \times \mathbf{H} = -i\omega \epsilon \mathbf{E} \quad (2.12)$$

$$\epsilon = \epsilon_0(1 + \chi) + i\frac{\sigma}{\omega} \quad (2.13)$$

It is important that all material properties enter into our final equations through the complex electric permittivity ϵ and the magnetic permeability μ . By taking the curl of (2.11) and (2.12), using the double-curl vector identity and assuming that $\nabla \cdot \mathbf{E} = 0$, it is found that both the electric and magnetic fields must satisfy the Helmholtz equation

$$\nabla^2 \mathbf{E} + k^2 \mathbf{E} = 0 \quad (2.14)$$

$$\nabla^2 \mathbf{H} + k^2 \mathbf{H} = 0 \quad (2.15)$$

where $k^2 = \omega^2 \epsilon \mu$. These vector wave equations are precise for well-separated particles and hold true both in the limit of very small spheres where the electrostatic equations apply, called the non-retarded case, and the general problem that considers wave retardation effects [32].

2.4 Surface Modes in Spheres, General Solution

Spheres that experience both spatial and temporal electromagnetic field variations experience retardation effects, which result in the surface-plasmon resonances being both shifted and broadened and the appearance of higher order multipolar mode excitations that lead to multiple resonance peaks. The quadropolar mode becomes notable at cluster diameters on the order of 80 nm and larger [28].

As noted earlier, neither propagating transverse nor longitudinal waves exist at frequencies below the plasma frequency, which for most metals is true at frequencies lower than the ultraviolet spectrum. In the Helmholtz equation, k can be found to equal the wave propagation constant $\sqrt{\epsilon_c} \frac{\omega}{c}$ and all solutions are transverse waves because $\nabla \cdot \mathbf{E} = 0$. To find the two independent transverse solutions of the electric field (TE) and the magnetic field (TM), we can reduce the problem from a vector one to a scalar one with well known solutions and then use them to solve the vector Helmholtz equation. The scalar Helmholtz equation is

$$\nabla^2 \psi + k^2 \psi = 0 \quad (2.16)$$

with solutions

$$\psi_{lm} = j_l(kr) Y_l^m(\theta, \phi) \quad l = 1, 2, 3, \dots \quad m = 0, \pm 1, \dots, \pm l \quad (2.17)$$

where j_l is a spherical Bessel function of the first kind and Y_l^m is a spherical harmonic. Solutions to the vector Helmholtz equation can be obtained from the scalar solutions, and are of the form

$$\mathbf{M}_l^m = \nabla \times (\mathbf{r} \psi_l^m) \quad (2.18)$$

$$\mathbf{N}_l^m = \frac{1}{k} \nabla \times \mathbf{M}_l^m \quad (2.19)$$

Additionally, \mathbf{M}_l^m and \mathbf{N}_l^m are related by

$$\mathbf{M}_l^m = \frac{1}{k} \nabla \times \mathbf{N}_l^m \quad (2.20)$$

The transverse electric (TE) modes, where the electric field is in the azimuthal direction and the magnetic field is in the radial direction, are given when $\mathbf{E} = A_l^m \mathbf{M}_l^m$ and $\mathbf{H} = -i A_l^m k \frac{c}{\omega} \mathbf{N}_l^m$. The transverse magnetic (TM) modes are obtained when $\mathbf{E} = B_l^m \mathbf{N}_l^m$ and $\mathbf{H} = -i B_l^m k \frac{c}{\omega} \mathbf{M}_l^m$. A_l^m , B_l^m and the field components both inside and outside the sphere can be obtained by satisfying the field continuity requirements at the boundary and the implicit requirements of the TE and TM modes.

After a significant amount of math, it can be shown that the TE modes do not have solutions when $\epsilon(\omega) < 0$ and no surface modes can exist [32]. The TM polariton modes are radiative, have a finite lifetime and can be excited by incident transverse magnetic plane waves. By taking the first few terms of the power series expansion of the TM solutions, it can be also be shown that their solutions agree with the electrostatic model at small dimensions.

The spherical characteristic equation, which can be solved to obtain the excitation frequency eigenvalues, is

$$\epsilon_o h_l(k_o R) [k_i R j_l(k_i R)]' = \epsilon_i j_l(k_i R) [k_o R h_l(k_o R)]' \quad (2.21)$$

where, j_l is a spherical Bessel function of the first kind, y_n is a spherical Bessel function of the second kind, h_l is a spherical Hankel function of first or second kinds, which are $j_l + iy_l$ and $j_l - iy_l$, respectively, and $'$ denotes differentiation with respect to the function arguments.

The scattering and absorption cross sections in units of the geometric cross section are

$$\sigma_s = \frac{2}{(k_o R)^2} \sum_{l=1}^{\infty} (2l+1) (|a_l|^2 + |b_l|^2) \quad (2.22)$$

$$\sigma_a = -\frac{2}{(k_o R)^2} \sum_{l=1}^{\infty} (2l+1) [(|a_l|^2 + |b_l|^2) + \text{Re}(a_l + b_l)] \quad (2.23)$$

where the net extinction of incident light is given by the sum of σ_s and σ_a . The Mie coefficients a_l and b_l are

$$a_l = -\frac{j_l(k_i R) [k_o R j_l(k_o R)]' - j_l(k_o R) [k_i R j_l(k_i R)]'}{j_l(k_i R) [k_o R h_l(k_o R)]' - h_l(k_o R) [k_i R j_l(k_i R)]'} \quad (2.24)$$

$$b_l = -\frac{\epsilon_o j_l(k_o R) [k_i R j_l(k_i R)]' - \epsilon_i j_l(k_i R) [k_o R j_l(k_o R)]'}{\epsilon_o h_l(k_o R) [k_i R j_l(k_i R)]' - \epsilon_i j_l(k_i R) [k_o R h_l(k_o R)]'} \quad (2.25)$$

As can clearly be seen, the complete theory is significantly more complicated than the simplified electrostatic at the limiting case of very small size. At the surface mode frequencies, the denominators of the Mie coefficients approach zero but are bounded by ϵ_i'' , which implies that materials should be selected for nanoplasmonics with very small imaginary dielectric function components at the Fröhlich mode frequency, which dominates at the small sizes.

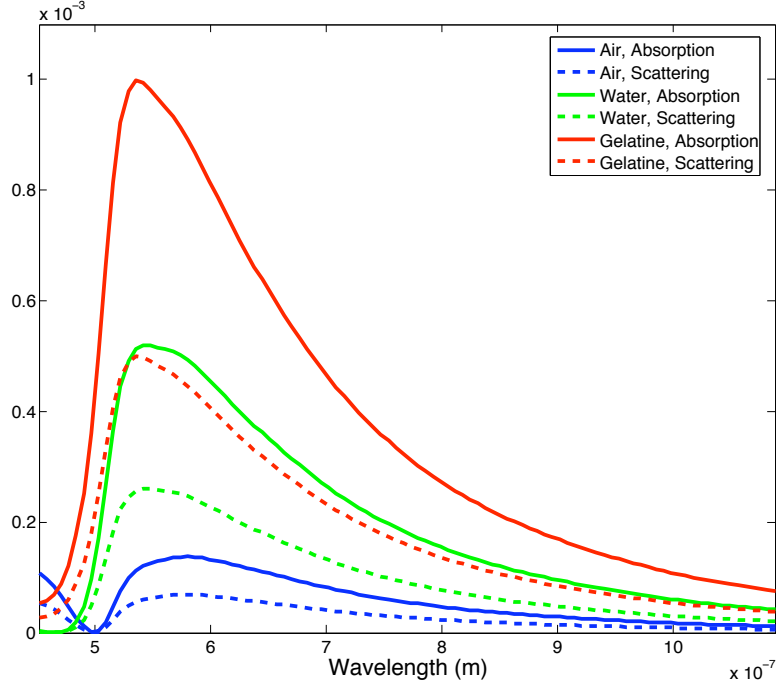


Figure 2.3: Calculated scattering and absorption spectra for 20 nm diameter gold spheres in various media using Mie theory in spherical coordinates.

The scattering and absorption spectra of 20 nm diameter gold spheres immersed in several solutions are shown in figure 2.3. The dipolar surface plasmon-polariton mode again dominates the mode profile. The dipolar mode frequency calculated by the exact Mie theory is higher than the frequency expected from the electrostatic approximation, shown in figure 2.2. The resonance intensity, frequency and width are dependent upon the dielectric function of the immersing medium and of the material complex dielectric function.

For gold and silver particles smaller than 50 nm, the first polarization normal mode dominates the higher order moments and absorption is the primary source of optical extinction [28]. Below 10 nm in diameter, the particle surface increasingly scatters light and the plasmon resonance is both broadened and reduced in magnitude [34].

Gold nanoparticles less than 10 nm in diameter absorb strongly in the green, and a solution of such nanoparticles will appear red. As their size increases, the plasmon resonance shifts into the red and they begin to appear blue. Scattering is weak for

particles less than about 50 nm, but red light is the dominant scattered wavelength due to the high scattering cross section at the resonance frequency. At larger sizes they appear slightly reddish due to the dominance of a broad scattering peak and their useful plasmonic properties are quenched.

2.5 Surface Modes in Infinite Cylinders

Infinite cylinders are of particular interest because their simple geometry can be numerically simulated and results can rapidly be compared with theoretical computations (Fig. 2.4). Complex two dimensional simulation structures, such as the nanocrescent, can only be simulated in two dimensions for a number of reasons that will be addressed later.

The method of solving the cylindrical case is very similar to the spherical case with a few differences. First, the scalar solution is of the form

$$\psi_n^h = J_n(\lambda r) e^{in\phi} e^{ihz} \quad (2.26)$$

where r , ϕ and z are the cylindrical coordinates and J_n is a Bessel function of the first kind. $\lambda = \sqrt{k^2 - h^2}$, where $h = 0$ for normally incident light, which will be of primary interest to us because that is the only case when pure TM and TE modes exist independently. The purpose of the two dimensional theory is to have a simplified testbed for analyzing numerical simulations and actual experiments will always involve spherical geometry, where only TM modes are supported. Thus, we will focus on the TM modes in cylindrical coordinates, or equivalently, our excitation light will always be normally incident upon the cylinder. Only radiative polariton modes will exist for this arrangement, which means that they will always be excitable as in the spherical case.

The characteristic equation for the cylindrical TM mode is of the form

$$k_i J_n'(k_i R) H_n(k_o R) = k_o J_n(k_i R) H_n'(k_o R) \quad (2.27)$$

where again, J_n is a Bessel function of the first kind, Y_n is a Bessel function of the second kind, H_n is a Hankel function of the first or second kinds, which are $J_n + iY_n$ and $J_n - iY_n$, respectively, and $'$ denotes differentiation with respect to the function arguments.

The scattering and absorption efficiencies are given as

$$Q_s = \frac{2}{k_o R} \sum_{n=-\infty}^{\infty} |a_n^p|^2 \quad (2.28)$$

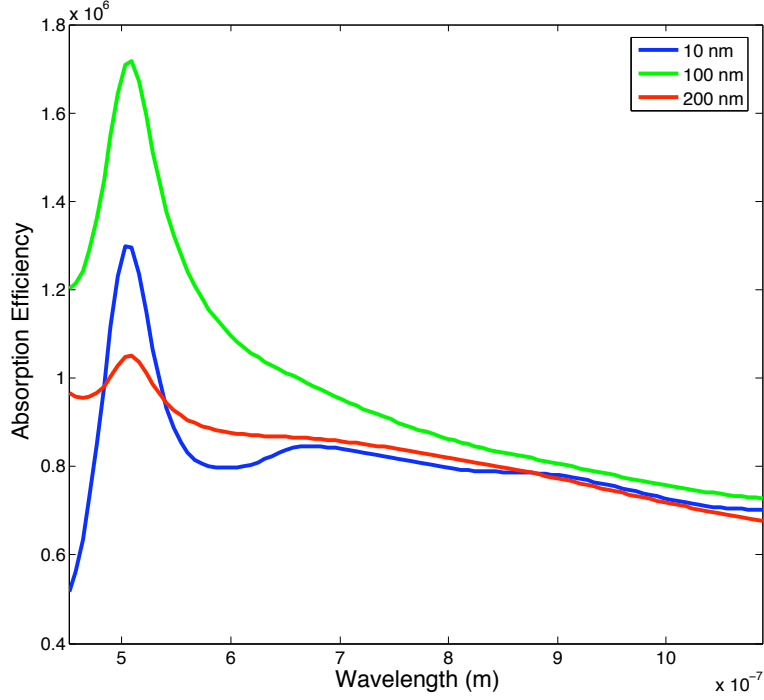


Figure 2.4: Calculated absorption spectra for gold cylinders of various diameters in air of using Mie theory in cylindrical coordinates.

$$Q_a = \frac{2}{k_o R} \sum_{n=-\infty}^{\infty} -(\text{Re}(a_n^p) + |a_n^p|^2) \quad (2.29)$$

where a_n^p for the incident TM light polarization case (\mathbf{E} in the radial direction, \mathbf{H} in the z direction) is of the form

$$a_n^p = -\frac{k_o J'_n(k_i R) J_n(k_o R) - k_i J_n(k_i R) J'_n(k_o R)}{k_o J'_n(k_i R) H_n(k_o R) - k_i J_n(k_i R) H'_n(k_o R)} \quad (2.30)$$

These cylindrical equations are dramatically simpler than their spherical counterparts, and are easily to numerically solve. The absorption spectra of gold cylinders of various diameters in air are shown in figure 2.4.

2.6 Propagating Surface Plasmon Polaritons in Thin Metal Films

Maxwell's equations in a linear isotropic, homogenous, non-magnetic medium with no charge or current take a particularly simple differential form

$$\nabla \cdot \mathbf{E} = 0 \quad \nabla \times \mathbf{E} = -\frac{\partial \mathbf{B}}{\partial t} \quad (2.31)$$

$$\nabla \cdot \mathbf{B} = 0 \quad \nabla \times \mathbf{B} = \epsilon \frac{\partial \mathbf{E}}{\partial t} \quad (2.32)$$

Solving (2.31) for the wave equations yields

$$\nabla^2 \mathbf{E} - \frac{\epsilon}{c^2} \frac{d^2}{dt^2} \mathbf{E} = 0 \quad (2.33)$$

$$\nabla^2 \mathbf{B} - \frac{\epsilon}{c^2} \frac{d^2}{dt^2} \mathbf{B} = 0 \quad (2.34)$$

Solutions to (2.33) include plane waves of the form $Ae^{-i(kr-\omega t)}$ with frequency ω and wave propagation vector k where $k^2 = \epsilon^2(\omega) \frac{\omega^2}{c^2}$. It can be seen that when $\epsilon(\omega)$ is negative, the propagation vector becomes imaginary and no propagating modes in the metal exist. However, surface plasmon polaritons that are bound to the metal surface are still valid solutions to Maxwell's Equations in this regime and are characterized by large localized electric, magnetic and polarization fields near the surface that exponentially decay away from it. TM waves are sometimes called p-polarized light in optics while TE waves are known as s-polarized light. At SPR, the TM component of the incident wave couples with the metal surface to form a propagating surface-plasmon polariton and is detected by a drastic reduction in the TM reflected light [35].

Consider the following solution at the plane boundary interface of two media where the surface normal is in the $+z$ direction, the incident wave direction is in the $+y$ direction, the interface is at $z = 0$, and the dielectric constants above and below the surface are ϵ_o and ϵ_i respectively. The real components of the dielectric constants determine the validity of the solution while the imaginary components determine the attenuation of the surface plasmon polariton.

$$z \geq 0$$

$$\begin{aligned} E_x &= E_0 e^{i(kx - \omega t)} e^{-z \sqrt{k^2 - \epsilon_o \frac{\omega^2}{c^2}}} \\ E_y &= 0 \\ E_z &= ik E_0 \sqrt{k^2 - \epsilon_o \frac{\omega^2}{c^2}} e^{i(kx - \omega t)} e^{-z \sqrt{k^2 - \epsilon_o \frac{\omega^2}{c^2}}} \end{aligned}$$

$$z \leq 0$$

$$\begin{aligned} E_x &= E_0 e^{i(kx - \omega t)} e^{z \sqrt{k^2 - \epsilon_i \frac{\omega^2}{c^2}}} \\ E_y &= 0 \\ E_z &= -ik E_0 \sqrt{k^2 - \epsilon_i \frac{\omega^2}{c^2}} e^{i(kx - \omega t)} e^{z \sqrt{k^2 - \epsilon_i \frac{\omega^2}{c^2}}} \end{aligned}$$

These solutions satisfy the wave equations and propagate along the surface at $z = 0$. However, additional constraints must be applied. First, the electric field must exponentially decay away from the surface, which is true if:

$$\sqrt{k^2 - \epsilon_o \frac{\omega^2}{c^2}} > 0 \quad \text{and} \quad \sqrt{k^2 - \epsilon_i \frac{\omega^2}{c^2}} > 0 \quad (2.35)$$

Additionally, the tangential components of \mathbf{E} and \mathbf{B} at $z = 0$ must be equal to ensure the continuity of the fields. E_0 can be chosen arbitrarily to satisfy the electric field requirements, while the \mathbf{B} component equations will determine k and ω . The magnetic field component equations are the same as those of the electric field with an additional factor of ϵ , so

$$\epsilon_o \sqrt{k^2 - \epsilon_o \frac{\omega^2}{c^2}} > 0 \quad \text{and} \quad -\epsilon_i \sqrt{k^2 - \epsilon_i \frac{\omega^2}{c^2}} > 0 \quad (2.36)$$

Solving for k and ω yields the following two equations.

$$k^2 = \frac{\omega^2}{c^2} \frac{\epsilon_o \epsilon_i}{\epsilon_o + \epsilon_i} \quad (2.37)$$

$$\omega^2 = (ck)^2 \left(\frac{1}{\epsilon_o} + \frac{1}{\epsilon_i} \right) \quad (2.38)$$

Several conclusions can be drawn from these results. From (2.35) and (2.36), $\epsilon_i < 0$ and from (2.37), $|\epsilon_i| > |\epsilon_o|$ for k to be real and the solution to be valid.

Up to this point we have not made any assumptions about medium i or o. If we let the former be air and the latter be a metal, then we can solve for the dispersion relation in more detail. By plugging (2.1) into (2.37) for ϵ_i and solving for k , the following momentum-frequency relation is obtained

$$k^2 = \frac{\omega^2}{c^2} \frac{\epsilon_o(\omega^2 - \omega_p^2)}{\omega^2(\epsilon_o + 1) - \omega_p^2} \quad (2.39)$$

This contrasts with the dispersion relation for electromagnetic waves in a dielectric medium with refractive index $n(\omega)$, $k = \frac{\omega}{c}n$.

Through numerical solution it can be shown that the momentum of the surface plasmon, $\hbar k_{sp}$ is greater than that of a photon of the same frequency, $\hbar k_0$. In order to generate coupled surface plasmon polaritons, the momentum of the photon and surface mode must be matched. There are several techniques for doing so. The first is to coat the thin metal film onto a high refractive index dielectric such as a prism. The prism increases the momentum of the incident light by a factor of n , and when the light strikes the thin film it will tunnel through, satisfying the momentum matching condition at the interface on the opposite side of the light source at a specific angle and will result in a propagating surface plasmon-polariton at that interface. The second is to scatter the light from subwavelength surface defects to generate local surface plasmons. The third, and oldest, technique is to use ruled metal gratings to generate surface plasmons.

A propagating surface plasmon polariton generally is not radiative due to the momentum matching condition. There are two benefits to transferring electromagnetic energy in the form of propagating surface plasmon-polaritons. First, energy can be transferred via nanostructures that significantly smaller than the diffraction limit, which is of important for producing photonic devices from silicon, which is currently a heavily researched topic. The second benefit of using plasmonic wave guides is a reduction in generated thermal energy due to radiative losses, which are negligible from surface plasmon-polaritons due to the momentum matching conditions.

Surface plasmon-polaritons were first observed in thin metallic films in 1957, and thin film systems continue to be an important topic with numerous applications including optoelectronic waveguides and biological sensors [36]. Thin metal films are generally functionalized and the binding of molecules can be detected as changes in the incident angle that meets the momentum matching conditions.

As noted earlier, the imaginary component of the dielectric constant determines the propagation length of the surface plasmon polariton. In a two-layer system it has been found to be [37].

$$\delta_{sp} = \frac{c}{\omega} \left(\frac{\epsilon'_i + \epsilon_1}{\epsilon'_i \epsilon_o} \right)^{\frac{3}{2}} \frac{(\epsilon'_i)^2}{\epsilon''_i} \quad (2.40)$$

where ϵ_o is assumed to be purely real. Propagation lengths for silver are on the order of 10-100 μm in the visible spectrum and can reach 1 mm in the near-infrared [38].

Chapter 3

Numerical Simulations

3.1 Software and Hardware Specifications

FEMLAB 3.1, a finite element analysis software package, and MATLAB 7.0, a scientific programming environment, were used in all simulations. FEMLAB is specifically designed to integrate with MATLAB through a programming interface that uses the MATLAB programming language. A number of simulation environments are included with FEMLAB including structural engineering, chemical engineering and electromagnetism modules. Simulations with coupled interactions between multiple physical domains, called multiphysics simulations, are supported and readily available. The simulations used in this paper were performed in both two and three dimensions and the computational mesh in each situation was generated using triangular elements and three-dimensional polyhedra, respectively. In both cases, the simulations were run on a single 2Ghz Pentium 4 processor with 2 GB of memory, 60,000 mesh elements on average and several hundred thousand degrees of freedom were typically used in each simulation. FEMLAB adaptively modified the mesh parameters to selectively reduce the element size at regions of high curvature to meet user configured parameters.

In the optical simulations, the local field enhancement factor was calculated by solving the two-dimensional Helmholtz equations within a rectangular domain of varying size with low-reflection boundary conditions to minimize any anomalous effects. The left-side of the computational domain emitted a transverse magnetic polarized electromagnetic field of unit strength. The sharp-tips of the gold nanocrescent were filleted to a radius of .25 nm to avoid field singularities and accurately model physical reality. All field retardation effects are fully realized in these simulations. Optical simulations were only performed in two dimensions because it is

significantly more difficult to fillet the sharp tips in three dimensions and the simulations would take at least an order of magnitude more time and memory to generate comparably accurate results.

The optical responses of the various materials studied is encoded in their complex dielectric functions. Interband electron transitions and other nonlinearities lead to the requirement that accurate experimental data, rather than theoretical models, be used for all numerical simulations. The experimental data collected by P.B. Johnson and R. W. Christy from thin films for gold and silver, was utilized in all optical simulations [31] and the iron optical data was taken from Weber [39] for the multilayer nanocrescent.

In the magnetic simulations, both two-dimensional and three-dimensional computational domains were used. A permanent bar magnet was situated relative to the ferromagnetic core in the case of the three-dimensional simulations, and the complete multilayer structure in the case of the two-dimensional simulations. The strength of the magnet was adjusted to obtain the desired magnetic flux density of approximately .1T, which corresponds to a relatively strong bar magnet. The two-dimensional and three-dimensional Maxwell surface stress tensors were solved for and integrated about the center of mass to calculate the torque and force vectors. The relative permeability of the iron layer was assumed to be 5000.

As with the theoretical calculations, all numerical simulation source code is included in the Appendix and additional information is provided there.

3.2 The Programming Interface

Although FEMLAB has an excellent graphical interface, setting up simulations using the MATLAB programming interface has a number of benefits, including greater speed, modularity, reproducibility and size. The computational of results, such as the maximum electric field, can be automatically simulated and collected whereas the graphical interface requires that both actions are performed manually, resulting in a several orders of magnitude increase in speed in practice. Additionally, MATLAB functions can be integrated into simulations for a more organized and object-oriented simulation environment. Settings are easier to maintain and modify based upon global variables using the programming interface and file sizes are on the order of 10^4 times smaller than the comparable files generated by the graphical interface due to extra information that is stored. Additionally, parametric simulations that study the effect of both geometry modifications and system parameters such as incident wavelength are only available through the MATLAB programming interface.

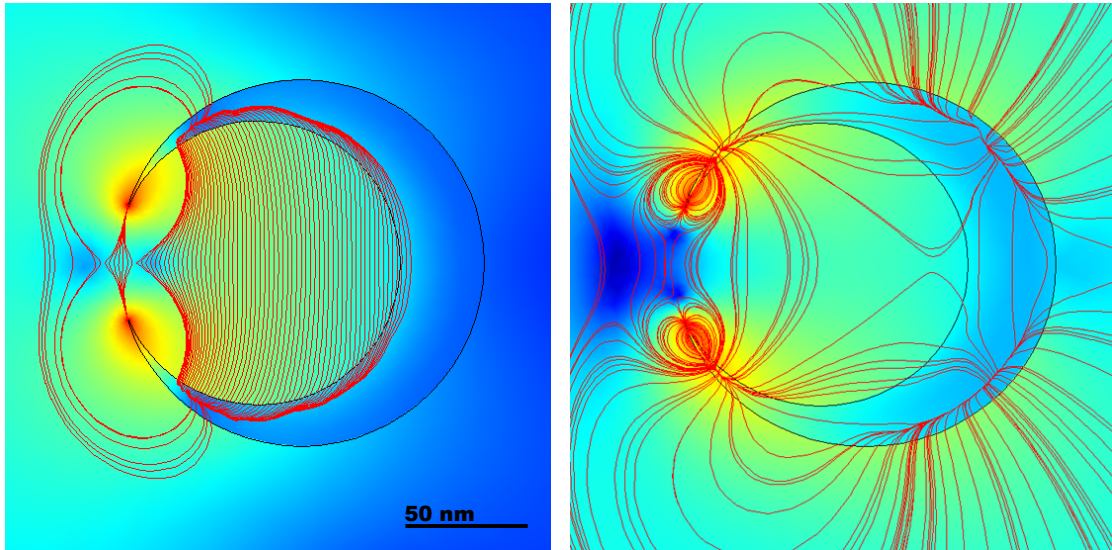


Figure 3.1: The dipolar and quadrupolar field profiles of the 200 nm outside diameter gold nanocrescent in air.

In hindsight, the benefits of the programming interface over the graphical interface are numerous and absolute and the decision to invest the time to learn the programming language was an excellent one.

3.3 Nanocrescent Optical Properties

The plasmon resonance and local field enhancement (LFE) of the homogenous nanocrescent depends upon its geometric parameters and upon the electromagnetic properties of the material used. The nanocrescent structure has been fabricated as a composite structure of multiple metal layers to demonstrate novel magnetic properties. Additionally, the plasmon resonance and LFE depend upon the orientation of the nanocrescent with respect to the incident light, being greatest when the light is polarized parallel to the sharp tips. The surface plasmon-polariton modes at both the inside diameter and outside diameter can be excited, and they will be referred to as the cavity and surface modes, respectively. The overall response of the nanocrescent is the result of coupling between the cavity and surface modes, primarily at the sharp tips via surface charges and short-range field interactions.

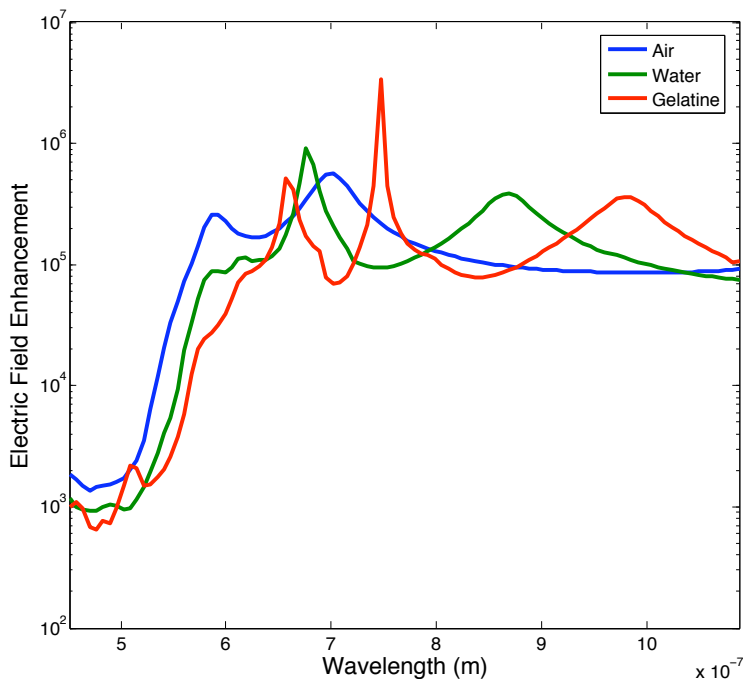


Figure 3.2: Local Field Enhancement spectra for a 200 nm outside diameter gold nanocrescent in various media.

The optical properties of the gold nanocrescent are useful for both biosensing through plasmon resonance shifts and for SERS. As noted earlier, the field enhancement of the gold nanoshell is on the order of 10^2 , while simulations indicate that field enhancement of the gold nanocrescent is on the order of 10^7 at dipolar resonance. Experimental data for the nanocrescent structure indicates a LFE on the order of 10^6 based upon SERS signal enhancement [40].

The LFE spectra of a gold nanocrescent with 150 nm inside diameter, 200 nm outside diameter and 72 nm nominal opening aperture diameter in a number of different media are plotted in figure 3.2. The shift of the dipolar resonance frequency to longer wavelengths in media with higher dielectric functions can be seen. The dipolar peak of the gold nanocrescent in water is at nearly 900 nm which is well within the NIR window of biological systems and solutions. The resonance shift shown is significantly greater than the shift expected from Mie theory in spherical nanoparticles, shown in figure 2.3. The larger than expected shift reflects the increased sensitivity of nanoplasmonic probes compared to colloidal nanoparticles and

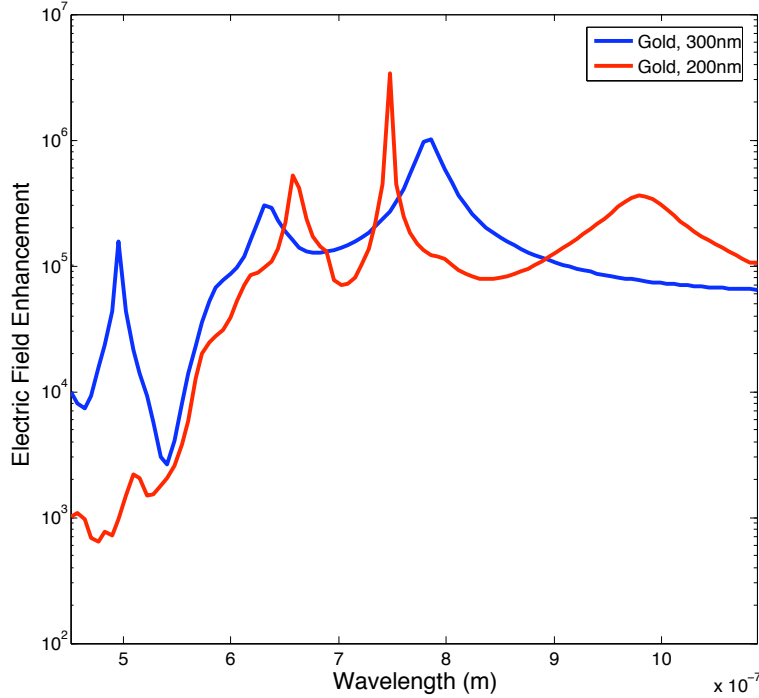


Figure 3.3: Local Field Enhancement spectra for 200 nm and 300 nm outside diameter gold nanocrescents in gelatine.

their particular relevance to quantitative biology. Higher order peaks become clearly visible in the water and gelatine solutions and they are at higher frequencies than the dipolar mode as expected.

The electric field profiles of the 200 nm outside diameter nanocrescent in air at the 590 and 700 nm resonance peaks are shown in figure 3.1. The 700 nm peak is clearly a dipolar mode, with a uniformly polarized cavity and field coupling between the sharp tips. The more complicated field profile of the 590 nm peak can be interpreted as the quadrupolar resonance mode. Surfaces where the plotted field streamlines begin and end are charged because $\nabla \cdot \mathbf{E} \neq 0$ at those points. The overall optical response of the nanocrescent depends upon the various coupling mechanisms and is not as easily interpreted as the well defined modes of spherical nanoparticles. In general, nanoplasmonic probe designs are still immature both to their recent conception and due to the variety of structures currently being explored.

The nanocrescent structure has not been thoroughly optimized to reduce the

width of the resonance peaks and increase their intensity. Only preliminary work has been completed to shift the peaks further into the NIR biological window. The ideal nanocrescent characteristics are different for the two modes of probe operation discussed in this paper. A SERS probe requires the efficient absorption and transformation of incident energy into an enhanced local field. The essential characteristic of a SERS probe is a large maximum field enhancement that is in the NIR window. A nanoplasmonic probe for biological sensing and bioassays can be used to optically detect changes in the local refractive index, indicative of changes in concentrations of both free and bound biomolecules. The latter type of probe again requires a peak in the NIR window, however scattered light is detected in this case and the probe sensitivity depends upon the width of the peak, not necessarily upon its overall intensity unless there is a significant amount of background noise. In both sensor roles for the nanoplasmonic

The simulated nanocrescent has not been thoroughly optimized to reduce the width of the resonance peaks and shift them further into the NIR biological window. Qualitatively, two possible avenues to these goals would be to reduce the width of the nanocrescent opening to increase the field coupling between them, which has been reported to be a dominant characteristic of the nanocrescent geometry [41]. The opening width is controlled by the fabrication process and increasing the angle of the substrate relative to the metal source during rotational deposition may be possible.

The field enhancement spectra of two gold nanocrescents with 150 nm inside diameter, 72 nm nominal opening aperture in gelatine with outside diameters of 200 nm and 300 nm are plotted in figure 3.3. Although the cavity modes and degree of coupling between the sharp-tips are identical between both structures, the change in the outside diameter dramatically modifies the resonance behavior of the 300 nm nanocrescent. The three nanocrescent geometric parameters are very closely coupled, and the overall system is very sensitive to change. Modifications to the nanocrescent geometry provide another pathway for the nanoplasmonic detection of biochemical processes. Although these possibilities have not been explored by the author, mechanical control systems for biological processes have been demonstrated, including the allosteric control of the maltose enzyme [42].

To shift the resonance peaks to longer wavelengths, the inner and outer cavities should be modified, however simulations have shown that they can not as a general rule be increased or decreased to engineer the nanocrescent properties. The resonant cavity and surface modes can be independently calculated using equations (2.21) and (2.27), however the effect of the coupling has not been quantified. Based upon table 2.1, silver would be an ideal material to improve the plasmon resonance strength and

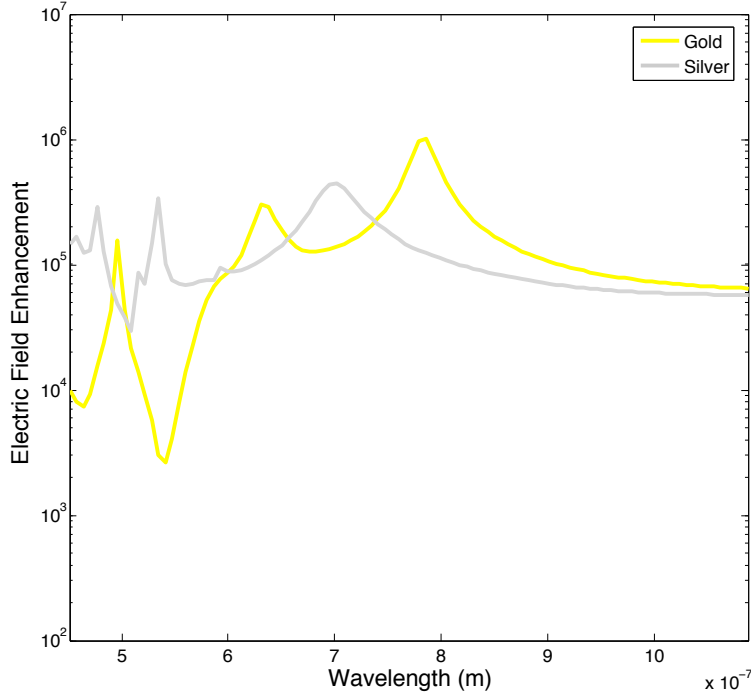


Figure 3.4: Local field enhancement spectra for 300 nm outside diameter gold and silver nanocrescents in gelatine.

width, however it is easily oxidized and is not a viable substrate for biocompatible nanoplasmonic probes unless it is coated with a coherent biocompatible thin film. Composite gold and silver nanocrescents have been investigated, however they have not been optimized and results are not available yet.

As with modifications to the geometric parameters, the local field enhancement spectra of silver and gold nanocrescents for the same geometry are drastically different as seen in figure 3.4. As with modifications to the geometric parameters, the nanocrescent system is very sensitive to the electromagnetic properties of the base material and the parametric optimization requires a significant amount of computing power and time for good results. The dipolar peak in figure 3.4 occurs in silver at 700 nm and gold at 800 nm and in general the resonance peaks for silver nanoplasmonic probes will be blue shifted relative to those of gold.

The four layer gold, iron, silver and gold nanocrescent, which will be discussed in section 3.5, is shown being illuminated in air by a 780 nm electromagnetic wave

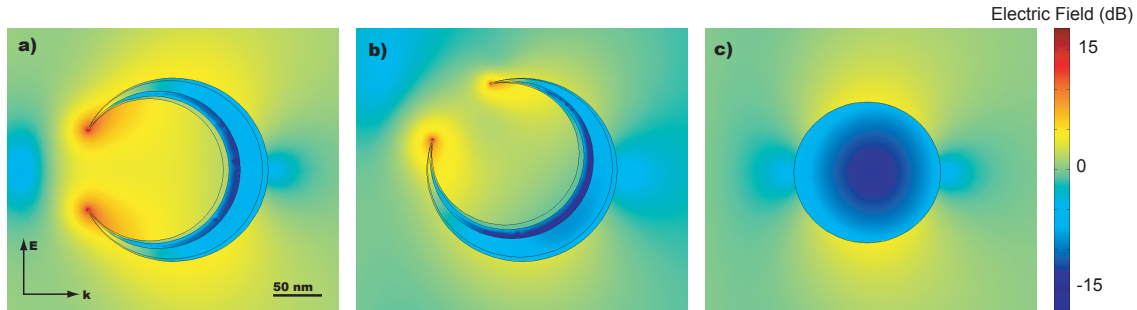


Figure 3.5: The four layer gold, iron, silver, gold nanocrescent and gold nanonanosphere with incident light from the left.

in figure 3.5. In 3.5a, the nanocrescent aperture is normal to the opening and the maximum field enhancement is shown in the dB scale with the color bar on the right. The nanocrescent is oriented at a forty-five degree angle to the incident wave in 3.5b, and the field enhancement is significantly reduced and localized at the tips. A 150 nm diameter gold sphere is shown in 3.5c under the same conditions and the field enhancement is dramatically reduced. The field enhancement of the sphere in 3.5c resembles that of a dipole, which indicates that the contributions of the higher order modes are negligible under these conditions.

3.4 Parametric Study of the Gold Nanocrescent Absorption Peaks

Extensive simulations have been performed on the gold nanocrescent structure by the author to empirically study the relationship between outside diameter, inside diameter, clear aperture and both the excitation mode wavelengths and intensities. The nanocrescent was considered to be in water for all simulations ($\epsilon_o = 1.79$) and 50 equally spaced excitation wavelengths from 451 to 1088 nm were simulated. The wavelength and value of the local field enhancement for the first three excited modes was numerically calculated from the simulation data. The resonance peak width was not quantified and will be studied in later work, although techniques for analyze the spectral width of the absorption and scattering peaks are currently being developed for another nanoplasmonic sensor research project by the author.

The first simulation study (Table 3.1) controlled the inside diameter for nanocre-

Table 3.1: Gold Nanocrescent Simulations - Results Summary

Outside Dia.	Inside Dia.	Clear Apert.	Dipolar		Quadrupolar		Hexapolar	
			λ	LFE	λ	LFE	λ	LFE
40	10	4.8	763	3.0e5	568	3.1e4	464	6.2e3
	20	9.6	958	2.4e6	607	7.3e5	490	2.7e4
	30	14.4	1088+	—	685	2.4e5	—	—
60	15	7.2	841	1.4e6	581	7.0e4	503	9.1e3
	30	14.4	1088+	—	646	5.0e5	—	—
	45	21.6	1088+	—	763	3.4e5	620	2.7e5
80	20	9.6	919	1.3e6	594	8.4e4	—	—
	40	19.2	1088+	—	685	2.9e5	581	5.6e4
	60	28.8	1088+	—	815	2.4e5	646	4.9e5
100	25	12	997	5.3e5	607	3.9e5	—	—
	50	24	1088+	—	711	8.6e5	594	2.8e5
	75	36	1088+	—	867	2.0e5	672	5.7e5
200	50	24	1088+	—	685	3.6e5	490	1.2e4
	100	48	1088+	—	828	1.0e7	646	1.0e5
	150	72	1088+	—	1049	1.8e6	802	5.3e5

scents with outside diameters ranging from 40 to 200 nm. The ratio of the inside diameter to the clear aperture remained constant to maintain the ratio of tip coupling to cavity size. As the inside diameter and clear aperture were increased the modes generally shifted to longer wavelengths. The shift was noticeably greater for the largest nanocrescents which can shift up to 400nm depending upon the cavity size. It should be emphasized that the opening width is directly proportional to the inside diameter and thus the relative intertip coupling is similar for the 200/50/24 and 100/50/24 or the 80/20/9.6 and 40/20/9.6 nanocrescents. However, the dipolar and quadrupolar modes of the 40/20/9.6 nanocrescent are noticeably shifted to longer wavelengths compared to the 80/20/9.6. Due to the negligible change in intertip coupling between the various simulated nanocrescents the force behind the shift must be related to the cavity and surface plasmon-polariton modes.

An increase in inside diameter is expected to red-shift the excitation modes however a reduction in outside diameter would be expected to blue-shift the modes if the cavity and surface modes are independent and do not interact. Two poignant examples of the red-shift with decreasing outside diameter can be seen when the quadrupolar mode shifts from 646nm in the 60/30/14.4 nanocrescent to 685nm in the 40/30/14.4 nanocrescent and when it shifts from 685nm in the 200/50/24 nanocres-

Table 3.2: Gold Nanocrescent Simulations - Detailed Results

Outside Dia.	Inside Dia.	Clear Apert.	Dipolar		Quadrupolar		Hexapolar	
			λ	LFE	λ	LFE	λ	LFE
200	50	12	1088+	—	698	2.1e5	503	2.9e4
		24	1088+	—	685	3.6e5	490	1.2e4
		48	1088+	—	620	3.7e7	490	1.0e5
200	75	18	789	5.9e5	620	2.5e5	516	4.2e4
		36	750	2.4e5	607	9.3e4	490	1.1e4
		72	659	8.6e5	477	4.7e3	451-	—
200	100	24	867	9.3e5	659	4.2e5	503	3.5e4
		48	828	1.0e7	646	3.0e6	490	1.0e5
		96	724	1.9e7	607	7.6e5	503	3.4e4
200	125	30	958	2.5e5	724	1.2e5	646	7.3e4
		60	919	2.5e7	711	9.4e6	633	4.6e6
		120	802	9.2e5	659	1.7e5	594	4.8e4
200	150	36	1075	3.8e5	815	1.5e5	750	3.3e4
		72	1049	1.8e6	802	5.3e5	698	1.0e6
		144	906	5.5e5	737	1.9e5	633	1.9e5
200	175	42	1088+	—	906	2.5e6	776	2.7e6
		84	1088+	—	932	1.4e6	802	2.0e6
		168	1088+	—	854	2.8e6	737	8.7e6

cent to 711nm in the 100/50/24 nanocrescent.

There are two factors which contribute to the red-shift with a reduction in OD or increase in ID. First, the overall wall thickness separating the cavity and outside surface is reduced which allows the electromagnetic fields of the cavity and surface modes to interact which shifts them to longer wavelengths and increases their intensity. The skin depth of gold at 800 nm is on the order of 2 nm and is less at longer wavelengths however some interaction is still to be expected between the inner and outer surfaces of the nanocrescent [43] [44]. Although the energy contained in the electromagnetic field is a maximum within the metal at the skin depth and decays exponential at greater depths, the field is non-negligible up to 30 nm within the metal from the incident surface and allows the surface modes in the cavity and on the surface to interact with one other. The other factor which supports an increase in excitation mode wavelength is the increased coupling between the cavity and surface modes at the tips based upon the thinner wall in that region. This view is supported by the existing understanding of the dominant nanocrescent electromagnetic

properties [41].

For a fixed outside diameter, the largest field enhancement was generated when the inside diameter was half the value of the outside diameter. However, the nanocrescent excitation modes shifted by up to several hundred nanometers toward the red when the cavity diameter was on the order of the overall nanocrescent diameter. The simulations demonstrate that the size of the polystyrene sphere template and thickness of the deposited material significantly affect the spectral position and intensity of the optically excited local electric field enhancement.

The 200nm nanocrescent was studied in more detail to determine the relationship between the clear aperture and excitation eigenmode wavelengths and to identify any clear empirical relationship between field enhancement and intertip coupling. While the resonance peaks were red-shifted with increasing inside diameter as with the previously noted simulation results, they shifted slightly towards shorter wavelengths with increasing clear aperture. The blue-shift can be attributed to two different factors. First, as the clear aperture increases for a fixed inside diameter the actual cavity surface area becomes smaller because it is clipped at the nanocrescent tips.

The spectral widths of the nanocrescent resonance modes have not been rigorously characterized at this time. However, preliminary data and graphical plots indicate that the full width at half maximum of the nanocrescent dipole mode can be as small as 5 nm. The sensitivity of the nanocrescent for SPR spectroscopy compared to the gold nanoshell is orders of magnitude better. As noted earlier in the paper, the full width at half maximum of single gold nanoshells is reported to vary from 1632 to 2298 nm. Further simulations and experiments are currently being planned to better characterize the gold nanocrescent and other nanoplasmonic probes for SPR spectroscopy, specifically by better measuring the spectral width of the resonance peaks and their sensitivity to changes in the local dielectric function due to adsorbed biomolecules.

In summary, the electromagnetic resonance peaks of the single layered gold nanocrescent can be tuned by controlling the geometric parameters during microfabrication. The inside, outside and open aperture diameters are controlled by the diameter of the polystyrene sphere template, the thickness of gold deposited and the deposition angle. The surface mode frequency depends strongly upon electromagnetic field interactions between the tips, the cavity and surface at the tips and the cavity and surface modes throughout the rest of the nanocrescent. As with other nanoplasmonic structures such as the nanoshell and nanoring, surface mode interactions lead to lower frequency resonance peaks with reduced spectral width. The gold nanocrescent possesses a number of surface plasmon modes with higher order modes at higher frequencies than the dipolar mode with generally lower local field enhancements. The

highest field enhancement is generally at the outside surface of the nanocrescent near the sharp tips which permits a spatial resolution on the order of tens of nanometers. Numerical simulations indicate that the plasmon resonance peaks can be tuned from 500-1100 nm with local electric field enhancement factors of up to 10^7 with a narrow spectral width for high sensitivity applications including SERS and label-free bioassays and sensors. Experiments confirm the simulation results with actual local field enhancement factors of up to 10^6 .

3.5 Magnetically Modulated Nanocrescent

The same fabrication process that is used to fabricate monolithic nanocrescent structures can be extended to multilayered structures and most metals. A magnetically modulated, four-layer nanocrescent has been fabricated from the deposition of gold, iron, silver and gold in that order on top of a monolayer of polystyrene beads. The magnetically modulated has been experimentally proven as a useful SERS substrate and publications are forthcoming [40]. Both gold and silver are diamagnetic, with relative permeabilities slightly less than unity, while the relative permeability of electron gun deposited iron is on the order of 5000. The gold, iron, silver and gold layers were 5, 10, 20 and 5 nm at maximum thickness. The ferromagnetic core was not magnetized before experiments or simulations, but tended to align itself anti-parallel to the magnet in both situations due to the asymmetric structure of the nanocrescent that places its center of mass away from the geometric center of a similarly sized sphere. There is a complete discussion of the properties and applications of the magnetically modulated nanocrescent in a paper by G. L. Liu et al. and this discussion will primarily discuss simulation results [40].

Due to the complexity of the complete structure, three-dimensional simulations were only performed on the iron core while two-dimensional simulations were performed on the complete structure. In two dimensions, simulations were run on both the iron core by itself and on the complete structure to discern the impact of the diamagnetic shell on the generated torque. Results were practically indistinguishable between the two sets of simulations and the effect of the diamagnetic shell was found to be negligible.

The torque on the nanocrescent varies as the sine of the angle between the incident magnetic field and the inward normal at the opening aperture, being zero at both parallel and antiparallel alignment. However, as in the analogous situation of a magnetic dipole in a uniform magnetic field, the antiparallel arrangement is unstable and the perturbed system will tend to align itself to the magnetic field.

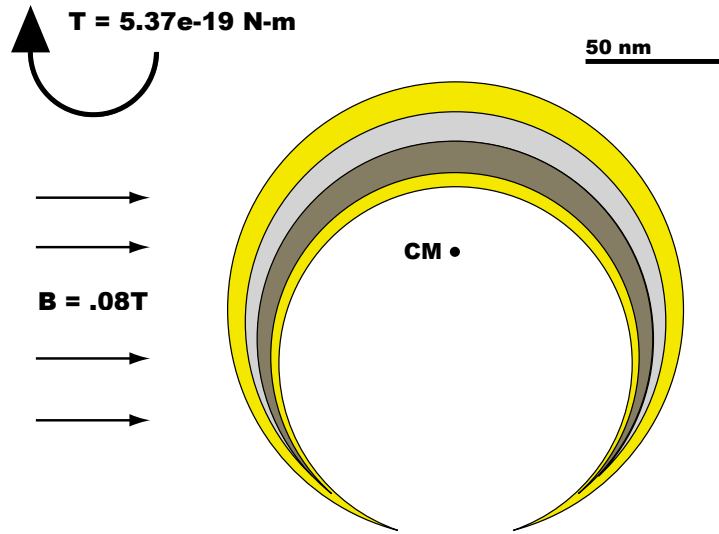


Figure 3.6: Graphical representation of the nanocrescent alignment for maximum torque, which is on the order of 10^{-19} N-m for the four-layer nanocrescent studied.

Magnetically modulated nanoplasmonic probes are of practical interest in self-assembled SERS arrays and in the alignment of asymmetric nanostructures, such as the nanocrescent, for optical signal generation [45] [46]. As noted earlier, the electric field enhancement of the nanocrescent structure is dependent upon its orientation with respect to the incident field. However, the primary reason that orientation control is of interest in nanoplasmonic probes, and especially asymmetric probes, is that the scattered field is a strong function of angle and can change with the adsorption of surface molecules. By rotating the incident magnetic field the Raman signal can be modulated to find the maximum signal-noise ratio.

The usefulness of simulations in the design of magnetically modulated nanoplasmonic probes and predicting their performance is limited. Although the gravitational and buoyancy forces on a probe suspended in a fluid are several orders of magnitude smaller, forces such as surface tension, liquid viscosity and Van der Waals interactions typically dominate at the nanometer scale and vary significantly based upon geometry and surface topology.

Chapter 4

Experiments

4.1 High Speed Spectral Imaging of Nanoplasmonic Probe Arrays

Surface plasmon resonance sensors are widely used to detect and characterize the biochemical dynamics of molecules immobilized on thin metallic films [47] [48] [49]. The abrupt change in reflectance of p-polarized light at onset of SPR (see section 2.6) can be implemented with a synchronized light source and sensor that rotate to find the characteristic angle, however this actuation technique is complicated, difficult to miniaturize and can not be multiplexed. Additionally, SPR sensor arrays with hundreds of test elements are currently the cutting edge of the technology, while microarrays with up to 10,000 elements are required for effective proteomics research [27]. Applications which conventional SPR sensor have been applied include measuring reaction rates, concentrations and high throughput drug screening by using large, lithographically patterned arrays on a solid substrate. The shift of the plasmon resonance frequency in nanoplasmonic probes provides another pathway for detection.

This semester I worked with a graduate researcher to implement a new, high speed spectra imaging system that can characterize thousands of nanoplasmonic probes within minutes, depending upon the wavelength band and spectral resolution required. Our spectral imaging system has frame rates as high as .5 frames per second and the spectroscopy of several thousand gold nanoparticles from 500 - 800 nm with a spectral resolution of 2 nm is demonstrated. Lithographically fabricated microarrays are also of particular interest in biomolecular screening and other *in vitro* applications, and the spectroscopy of a gold nanowire array is also demonstrated.

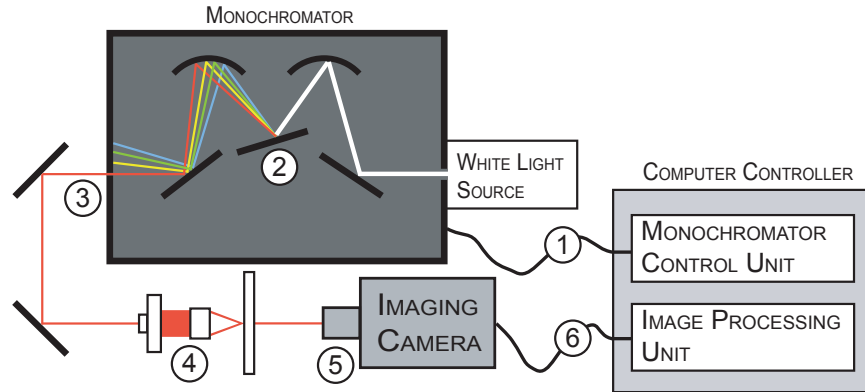


Figure 4.1: A summary of the experimental setup used in our spectral imaging system.

An overview of the experimental apparatus and procedure are shown (Fig. 4.1). In the figure, the monochromator control unit (1) moves the diffraction grating (2) to a set position to send a monochromatic light beam through the small exit slit (3). The output beam is directed by a series of mirrors and lenses to the microscope input, where it is passed through a beam expander and dark field condenser (4) onto the specimens. Only the scattered light passes on to the imaging camera (5) which takes a digital still image and passes the resulting black and white image to the image processing unit (6). Images are taken at a series of wavelengths and analyzed to produce scattering spectra of the specimens in the camera field of view.

Nanoplasmonic probe spectroscopy has been extensively studied in recent years as another potential pathway for the characterization of single biomolecules. The benefits of nanoplasmonic probe arrays over conventional SPR sensor arrays include a significantly smaller required sample volume, a greater potential for miniaturization and high throughput detection arrays, and greater sensitivity. However, nanoplasmonic probe spectroscopy has previously been limited to several particles due to limitations of the spectra imaging systems used. Previous systems have illuminated the sampled with white light via a dark-field condenser and send the scattered light into a monochromator and spectrometer in order to generate a scattering spectrum. However, such systems are limited by the size of the entrance slit to the monochromator, which is on the order of several microns, and by the potential crosstalk between

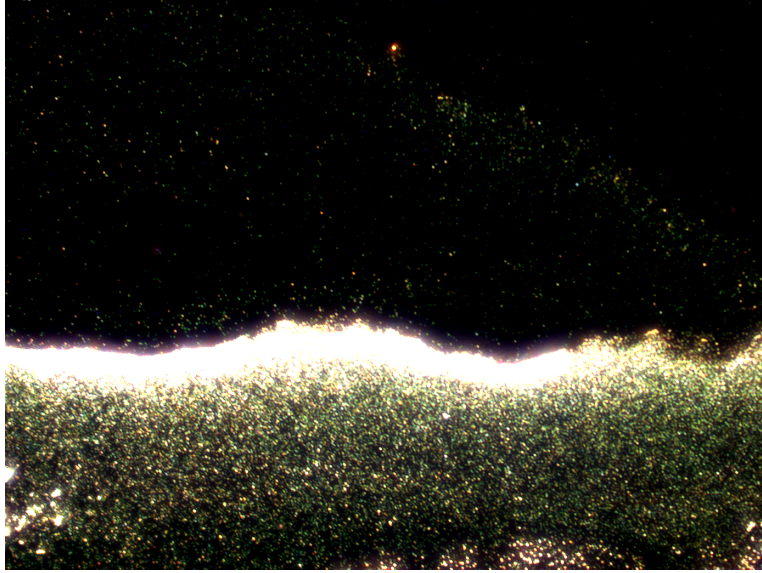


Figure 4.2: A true color image of the nanoparticle sample region analyzed.

adjacent nanoplasmonic probes which will render the generated spectrum useless. Spectrally imaging thousands of probes in an array is simply not feasible due to the human or computer intervention required to scan the sample stage to image each individual particle, which can shift the imaging immersion fluid and require that the microscope is refocused for each probe that is imaged. This raises questions regarding the accuracy of data obtained from such systems due to alignment and focus issues, but also due to the time span over required to image large arrays. Most biochemical reactions of interest take a number of minutes to several hours to be completed, however the discussed systems can take a significant fraction of that time to generate spectral image data which renders them useless in applications that require near real-time sensing.

Our spectral imaging system uses a 100 W halogen lamp light source which sends light into the monochromator via a narrow slit and is subsequently diffracted from a blazed diffraction grating. The monochromator is controlled by a software control unit that we wrote. The exit light beam has a spectral width of approximately 2 nm and a power density that varies from 100 - 300 $\frac{\mu W}{cm^2 nm}$. As can be seen, there are two mutual exclusive design goals in our system; to have a spectrally narrow output beam from the monochromator and to have a high incident power density on the nanoplasmonic probes being studied. Once the monochromatic beam enters the

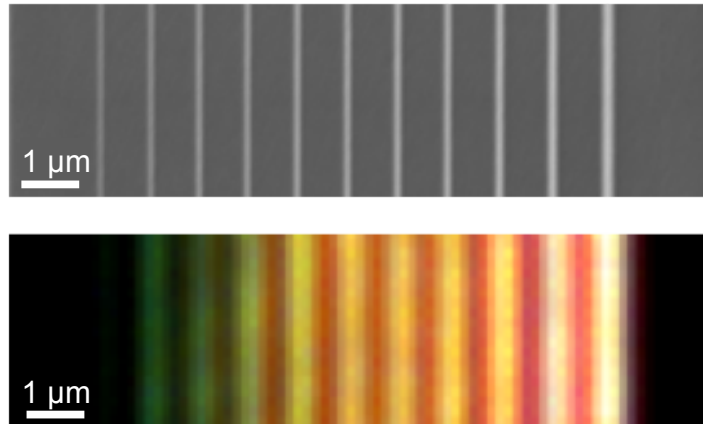


Figure 4.3: A scanning electron microscope (SEM) and true color image of the nanowires analyzed.

microscope it is focused onto the sample, which is immersed in deionized water, via a dark-field condenser. Dark-field condensers are designed such that the incident light strikes the sample from an oblique angle and only the scattered light passes through the objective lens and is detected by the camera. A 40x objective lens collects the scattered light which is sent to a 512 x 512 pixel CCD imaging camera and the data is formatted and saved by another software control unit for later analysis. The monochromator and camera control units are integrated into a single software package and are synchronized to capture a single image at each wavelength of interest. There are a number of input parameters to our control system, including spectral range, resolution and integration time, which determine the overall time required for spectroscopy. The field of view of our microscopy system is on the order of $300\ \mu\text{m}$ x $300\ \mu\text{m}$ and a 100×100 nanoplasmonic probe array could be clearly resolved and analyzed by our demonstrated microscopy unit without any need for sample stage scanning or complicated mechanical feedback control systems.

The experimental results for the gold nanoparticle and nanowire samples are shown in figures ?? and 4.5. The gold nanoparticle sizes ranged between 20 and 80 nm, with plasmon resonance peaks falling in the visible spectrum from blue to red. Three representative nanoparticles are shown and curves from the data are plotted with maximum scattering peaks in the green, yellow and red. The gold nanowires were previously fabricated by a graduate researcher to demonstrate the resonance tuning in one-dimensional nanostructures. The wire widths ranged between 20 and

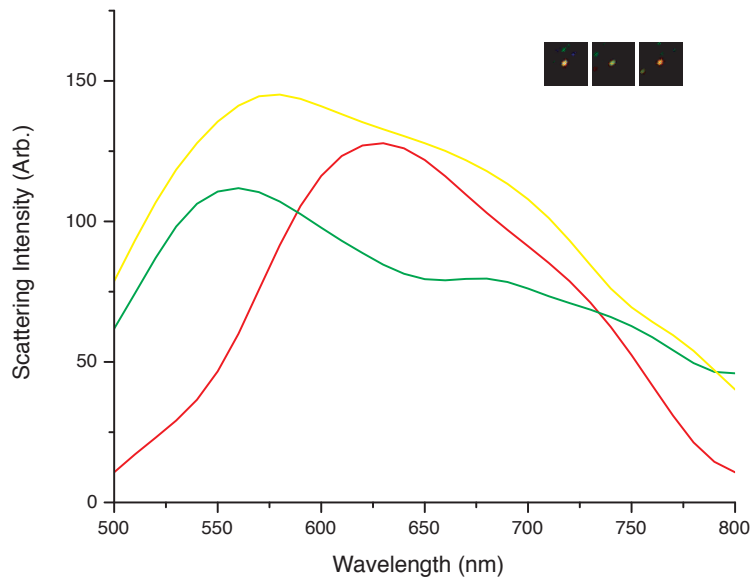


Figure 4.4: Experimental scattering spectra from the gold nanoparticle solution.

150 nm, with resonance peaks from the green to red. The spectral intensity of the red nanowires were greater than the green nanowires due to their significantly greater geometric cross section. The wires were imaged in oil and curves are plotted for wire widths of 60, 80 and 120 nm with peaks in the green, orange and red, respectively.

The diffraction grating and camera are controlled by software written in LabView and run from a desktop PC connected to our equipment via serial connections. Data analysis was performed in MATLAB and data visualization was performed in OriginPro. Image data is collected at each wavelength as an uncompressed, grayscale, 16-bit unsigned integer TIF and analyzed in MATLAB as a two-dimensional integer array. No noise reduction or smoothing algorithms are applied to the image data before analysis. The mean intensity of the image bright spots, which are typically only several pixels, is extracted at each wavelength and stored as the raw scattering spectra. The mean intensity value in a large, empty region is also extracted at each wavelength to serve as the background reference spectrum. The difference between the two spectra is inversely scaled by the light source spectrum to account for the variation in intensity in the light source spectrum. Using a high quality xenon lamp would render this last step unnecessary.

Our spectral imaging system demonstrates the feasibility of using nanoplasmonic

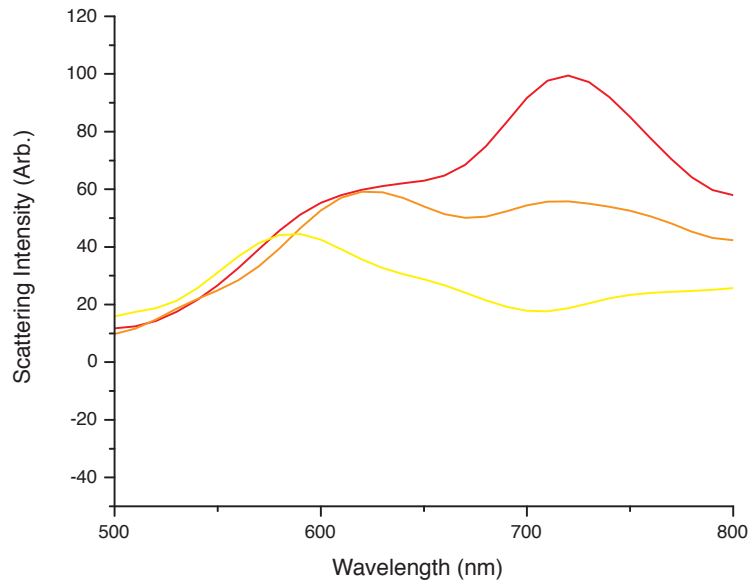


Figure 4.5: Experimental scattering spectra for 60, 80 and 120 nm wide gold nanowires.

probe arrays in very high throughput applications that require real-time or near real-time data, such as monitoring biochemical processes on the cellular level. The imaging times demonstrated are on the order of 5 minutes, which is several times better than other nanoplasmonic probe spectral imaging systems. By reducing the spectral resolution or range, which is acceptable when fabricated nanoplasmonic probes with well controlled resonance peaks are used, the speed could be increased significantly and real-time optical analysis of nanoplasmonic probe arrays could become a reality. Our system has significant potential for miniaturization, multiplexed sensing with a single illumination source and integration into microfluidic analysis systems for fields that require data with high statistical confidence, repeatability and parameter control such as proteomics.

Chapter 5

Future Goals

I have spent the past two semesters focusing almost purely upon learning theory and developing a finite element method programming framework for rapidly characterizing and optimizing the optical features of nanoplasmonic probes. Two papers that I have collaborated on are in the process of being submitted to journals and I hope to write a paper of my own on the topic of numerical simulations of nanocrescents and nanodot arrays for SERS and SPR spectroscopy. In my senior year I hope to design and perform more experiments and focus on bionanophotonics applications with well defined goals and presentable results. In general, my current research interests are in developing new laboratory tools and methods for biological analysis, with the ultimate goal of understanding the biochemical dynamics of the cell at the molecular level. I plan to graduate from UC Berkeley in the spring of 2006 with a B.S. in Mechanical Engineering and will apply to graduate school with an emphasis in systematic bioengineering with an emphasis on applied physics and quantitative biological sciences.

In the coming year I hope to focus on refining our spectral imaging analytical technique through experiments with microfluidic channel arrays and on the development of refined nanoplasmonic probes through numerical simulation and experimental demonstration. First, I would like to demonstrate the ability of the spectral imaging technique in conjunction with simple nanoplasmonic probes to detect the adsorption of specific biomolecules in solution. I am currently performing rigorous simulations characterizing the SPR spectroscopic properties of two dimensional gold nanodot arrays. The simulations have two purposes. First, they will be used to design a nanodot substrate that can be fabricated using electron beam lithography for my SPR spectroscopy experiments. Also, the simulation results will form a solid basis to write a paper on the unique electromagnetic properties of gold nanodot substrates

for SERS and SPR spectroscopy. As an extension of that concept, I would like to demonstrate the detection of conformational changes of adsorbed species after the introduction of enzymes at concentrations comparable to commercial SPR sensors with higher throughput, faster response and better automation capabilities.

In the realm of more advanced nanoplasmonic probes with narrow plasmon resonances and high local field enhancement, I would like to do several things. First, I would like to develop an optimized silver core, gold shell nanocrescent with an improved field enhancement in the NIR for *in vivo* SERS. Next, I want to develop a new nanoplasmonic probe geometry for production via top-down nanofabrication processes based upon basic theory and simulation results. Finally, and most importantly, I would like to integrate existing nanoplasmonic probes into arrays that take advantage of our very high throughput, automated, label-free spectral imaging system to demonstrate the immediate utility of the technology in studying the biochemical dynamics of the cell.

Appendix A

Theoretical Calculations Code

All code in the appendix is available under the GNU Free Documentation License 1.2 and is free to be modified and distributed within the limits of that license. Basically, you can modify and distribute all of this code with the restrictions that you give credit when due and that you distribute any modifications that you make to the source code whenever possible. All code is original, except for three functions posted on the internet by Dave Barnett from the Optical Engineering Group at Loughborough University circa 1996, which were used to calculate the Mie coefficients for spherical nanoparticles. I would appreciate feedback, even if you just say that the code was useful to you, and I would be happy to answer any questions or fix any errors that are found. You can contact me at jcdoll at gmail dot com.

The numerical simulation code must be run from the MATLAB command line after starting up the FEMLAB with MATLAB software package for full functionality. It may be opened directly from within FEMLAB so that you can view the geometry and extract images. However, MATLAB expressions will not be evaluated and before doing so you may want to set the number of iterations within the code to one and set the parameters to the values desired in order to reduce the time required.

This paper was written in TeXShop 1.35 and 2.0 on Mac OS X, which uses LaTeX for formatting and pdfLaTeX to output into .pdf format. LaTeX was installed using Fink and Fink Commander. The bibliography was produced in BibTeX. Adobe Illustrator was used to create and edit many figures, which were exported from FEMLAB as uncompressed .tif's and from MATLAB as .pdf's.

A.1 OpticalData.m

```
%{
```

Joseph Doll
OpticalData.m

Parameters:

lambda_start = Wavelength that output will start at, inclusive
lambda_end = Wavelength that output will end at, inclusive
lambda_step = Length of output vector, matl_eps
matl = Integer that indicates the output material.
1 = Gold, 2 = Silver, 3 = Iron

Return Values:

matl_eps = Vector of length lambda_step with the interpolated
dielectric function.
matl_n = Vector of length lambda_step with the interpolated
complex refractive index.
%}

```
function [matl_eps, matl_n] = OpticalData(lambda_start, ...  
lambda_end, lambda_step, matl)
```

```
%---Constants-----
```

```
h = 4.136e-15; % planck's constant in units of eV  
c = 3e8; % speed of light  
%-----
```

```
% Silver and Gold Optical Data: extends from 451nm through 1088nm.
```

```
eV_jc = [2.75 2.63 2.50 2.38 2.26 2.13 2.01 1.88 1.76 1.64 1.51 ...  
1.39 1.26 1.14];
```

```
wavelength_data_jc = h*c./eV_jc;
```

```
% Complex optical constants for Gold
```

```
au_n = [1.38 1.31 1.04 0.62 0.43 0.29 0.21 0.14 0.13 0.14 0.16 ...  
0.17 0.22 0.27];
```

```
au_k = [1.914 1.849 1.833 2.081 2.455 2.863 3.272 3.697 4.103 ...  
4.542 5.083 5.663 6.350 7.150];
```

```
% Complex optical constants for Silver
```

```
ag_n = [.04 .05 .05 .05 .06 .05 .06 .05 .04 .03 .04 .04 .04 .04];  
ag_k = [2.657 2.869 3.093 3.324 3.856 3.858 4.152 4.483 4.838 ...  
5.242 5.727 6.312 6.992 7.795];
```

```

% Iron Optical Data: extends from 443nm through 1128nm.
eV_fe = [2.8 2.7 2.6 2.5 2.4 2.3 2.2 2.1 2.0 1.9 1.8 1.7 1.6 1.5 ...
        1.4 1.3 1.2 1.1];
wavelength_data_fe = h*c./eV_fe;
% Complex optical constants for Iron
fe_n = [2.12 2.23 2.34 2.46 2.56 2.65 2.74 2.80 2.85 2.89 2.92 ...
        2.98 3.00 3.05 3.12 3.16 3.24 3.33];
fe_k = [3.23 3.25 3.30 3.31 3.31 3.34 3.33 3.34 3.36 3.37 3.46 ...
        3.52 3.60 3.77 3.87 4.07 4.26 4.52];

% Calculate n and the dielectric constant (epsilon) for
au_cn = au_n + i*au_k;
au_eps = au_cn.^2;
ag_cn = ag_n + i*ag_k;
ag_eps = ag_cn.^2;
fe_cn = fe_n + i*fe_k;
fe_eps = fe_cn.^2;

% Interpolation
lambda = linspace(lambda_start, lambda_end, lambda_step);
au_eps_r = interp1(wavelength_data_jc, real(au_eps), lambda, 'spline');
au_eps_i = interp1(wavelength_data_jc, imag(au_eps), lambda, 'spline');
au_n_r = interp1(wavelength_data_jc, real(au_cn), lambda, 'spline');
au_n_i = interp1(wavelength_data_jc, imag(au_cn), lambda, 'spline');

ag_eps_r = interp1(wavelength_data_jc, real(ag_eps), lambda, 'spline');
ag_eps_i = interp1(wavelength_data_jc, imag(ag_eps), lambda, 'spline');
ag_n_r = interp1(wavelength_data_jc, real(ag_cn), lambda, 'spline');
ag_n_i = interp1(wavelength_data_jc, imag(ag_cn), lambda, 'spline');

fe_eps_r = interp1(wavelength_data_fe, real(fe_eps), lambda, 'spline');
fe_eps_i = interp1(wavelength_data_fe, imag(fe_eps), lambda, 'spline');
fe_n_r = interp1(wavelength_data_fe, real(fe_cn), lambda, 'spline');
fe_n_i = interp1(wavelength_data_fe, imag(fe_cn), lambda, 'spline');

% Calculate the complex dielectric constants for the wavelengths of
% excitation that we are interested in.

```

```

au_eps = au_eps_r + i*au_eps_i;
au_n    = au_n_r + i*au_n_i;

ag_eps = ag_eps_r + i*ag_eps_i;
ag_n    = ag_n_r + i*ag_n_i;

fe_eps = fe_eps_r + i*fe_eps_i;
fe_n    = fe_n_r + i*fe_n_i;

if (matl == 1)
    matl_eps = au_eps;
    matl_n = au_n;
elseif (matl == 2)
    matl_eps = ag_eps;
    matl_n = ag_n;
elseif (matl == 3)
    matl_eps = fe_eps;
    matl_n = fe_n;
end;

```

A.2 ElectrostaticSpectra.m

```

%{
Joseph Doll
ElectrostaticSpectra.m
Plot the absorption spectrum of 20 nm diameter metallic
nanoparticles immersed in numerous media to illustrate
the resonance wavelength shift that can form the basis
of the nanoplasmonic probes.
%}

clf;
FEMLAB 3.1 simulation to calculate the maximum local electric field

lambda = linspace(451e-9,1088e-9,500);

% Dielectric function of the immersing medium
eps_o1 = 1; % Air

```

```

eps_o2 = 1.7875; % Water
eps_o3 = 2.37; % Gelatine

% Dielectric function of the metallic nanoparticle
eps_i = OpticalData(451e-9,1088e-9,500,1);

% Radius of the metal nanoparticle
R = 10e-9;

% Calculate the extinction cross sections per Kreibig
sigma_e1 = (54*pi^2./lambda).*(eps_o1^1.5*R^3.*imag(eps_i))./ ...
((real(eps_i)+2*eps_o1).^2 + imag(eps_i).^2);
sigma_e2 = (54*pi^2./lambda).*(eps_o2^1.5*R^3.*imag(eps_i))./ ...
((real(eps_i)+2*eps_o2).^2 + imag(eps_i).^2);
sigma_e3 = (54*pi^2./lambda).*(eps_o3^1.5*R^3.*imag(eps_i))./ ...
((real(eps_i)+2*eps_o3).^2 + imag(eps_i).^2);

hold on;
plot(lambda, sigma_e1, ...
      lambda, sigma_e2, ...
      lambda, sigma_e3);
legend('Air','Water','Gelatine');
ylabel('Extinction Cross Section');
xlabel('Wavelength (m)');
axis([451e-9 600e-9 0 3e-16]);
hold off;

```

A.3 SphereSpectra.m

```

%{
Joseph Doll
SphereSpectrum.m
Plots the scattering and absorption efficiencies for a cylinder immersed
in an outer medium. The optical properties of both materials can
be specified. Gold, silver and iron data is accessed from OpticalData.m
from 451 - 1088 nm. Incident light is TM polarized and only TM polariton
modes are excited.
%}

```

```

clf;

% Radius of the cylinder (m)
radius = 10e-9;

% Wavelengths that will be plotted
lambda = linspace(451e-9, 1088e-9, 100);

%Dielectric function outside the cylinder
eps_o = 2.37;
n_o = sqrt(eps_o);

% Dielectric function inside the cylinder
[eps_i, n_i] = OpticalData(451e-9, 1088e-9, 100, 1);

% Wave number inside the cylinder
k_i = 2*pi.*sqrt(eps_i)./lambda;

% Wave number outside the cylinder
k_o = 2*pi.*sqrt(eps_o)./lambda;

% Initialize the summation variables
Q_s = [];
Q_a = [];

% For each wavelength...
for ii = [1:length(lambda)]

    % Initialize our summation variables
    Sum_e = 0;
    Sum_s = 0;
    l_max = 50;

    % x = k_o*radius, m = n_i/n_o = sqrt(eps_i)/sqrt(eps_o)
    % ScatCoef from Dave Barnett, Loughborough University

    [a,b] = ScatCoef(real(n_i(ii))./n_o, k_o(ii)*radius, l_max);

```

```

% Calculate the values of the summations
for l = 1:l_max,
    Sum_s = Sum_s + (2*l + 1)*(abs(a(l))^2 + abs(b(l))^2);
    Sum_e = Sum_e + (2*l + 1)*(real(a(l) + b(l)));
end

% Append the scattering efficiency at this wavelength
Q_s = [Q_s 2./(k_o(ii)*radius)^2*Sum_s];
Q_a = [Q_a -2./(k_o(ii)*radius)^2*(Sum_e + Sum_s)];
end

% Plot!
hold on;
plot(lambda, abs(Q_s), 'r-');
plot(lambda, abs(Q_a), 'b-');
legend('Scattering Efficiency', 'Absorption Efficiency');
xlabel('Wavelength (m)');
ylabel('Effective Cross Section');
hold off;

% ScatCoef Scattering coefficients
% [a,b]=ScatCoef(m,x,nmax)
% returns the two column vectors a and b containing
% the scattering coefficients for particles of size x
% and refractive index relative to medium m, from n=1
% to n=nmax.

% Written by and copyright
% Dave Barnett
% Optical Engineering Group
% Dept. of Electrical and Electronic Engineering
% Loughborough University
% 20th November 1996

% Corrected 4th September 1997
% m missing from calculation of dphim

% 5th September 1997

```

```

% computation method optimised by use of vector methods

function [a,b] = ScatCoef(m,x,nmax)

N = (1:nmax)';
phi = RB1(x, nmax);
phim = RB1(m*x, nmax);
zeta = RB2(x, nmax);
xi = phi + i * zeta;
phin_1 = [sin(x);phi(1:nmax-1)];
phimn_1 = [sin(m*x);phim(1:nmax-1)];
zetan_1 = [-cos(x);zeta(1:nmax-1)];
dphi = phin_1-N.*phi/x;
dphim = phimn_1-N.*phim/(m*x);
dzeta = zetan_1-N.*zeta/x;
dxi = dphi + i * dzeta;
a = (m*phim.*dphi - phi.*dphim) ./ (m*phim.*dxi - xi.*dphim);
b = (phim.*dphi - m*phi.*dphim) ./ (phim.*dxi - m*xi.*dphim);

% RB1 the Ricatti-Bessel function of the first kind
% RB1(rho, nmax) for the value rho from n=1 to n=nmax.

% Written by and copyright
% Dave Barnett
% Optical Engineering Group
% Dept. of Electrical and Electronic Engineering
% Loughborough University
% 20th November 1996

function phi = RB1(rho, nmax)
nst = ceil(nmax + sqrt(101+rho));
phi(nst,1) = 0;
phi(nst-1,1) = 1e-10;
for n=nst-2:-1:1
phi(n,1) = (2*n+3)*phi(n+1)/rho - phi(n+2);
end
phi0 = 3*phi(1)/rho - phi(2);
phi0 = sin(rho)/phi0;
phi = phi(1:nmax,:) * phi0;

```

```
% RB2 the Ricatti-Bessel function of the second kind
% RB2(rho, nmax) for the value rho from n=1 to n=nmax.

% Written by and copyright
% Dave Barnett
% Optical Engineering Group
% Dept. of Electrical and Electronic Engineering
% Loughborough University
% 20th November 1996

function zeta = RB2(rho, nmax)
zeta(1,1) = -cos(rho)/rho - sin(rho);
zeta(2,1) = 3*zeta(1)/rho + cos(rho);
for n=3:nmax
zeta(n,1) = (2*n-1)*zeta(n-1)/rho - zeta(n-2);
end
```

Appendix B

Numerical Simulations Code

B.1 OpticalOneLayer.m

```
% Joseph Doll
% OpticalOneLayer.m
% FEMLAB 3.1 simulation to calculate the maximum local electric field
% enhancement for a gold or silver nanocrescent of arbitrary ID, OD,
% and opening width immersed in a low absorption dielectric medium of
% arbitrary dielectric constant.

flclear fem
clear vrsn
vrsn.name = 'FEMLAB 3.1';
vrsn.ext = '';
vrsn.major = 0;
vrsn.build = 157;
vrsn.rcs = '$Name: $';
vrsn.date = '$Date: 2004/11/12 07:39:54 $';
fem.version = vrsn;

% -----
% ----- Start Geometry Initialization -----
% -----

% Nominal opening width between tips (increased by fillet)
nc_open = 72e-9;
```

```

% Angle to rotate the nanocrescent for simulation
theta = 0;

% Radii of circles that define the nanocrescent layers
nc_outer = 100e-9;
nc_inner = 75e-9;
% Note that the circles will be shifted later, so thicknesses
% here are not exact.

% Calculate the horizontal displacement of each ellipse based
% upon the dimensions noted above (radii and opening widths)
nc_outer_x = 0;
nc_outer_y = 0;

nc_inner_x = -((nc_outer - nc_inner) + ...
(nc_inner*(1-cos(asin(nc_open/(2*nc_inner)))))) - ...
(nc_outer*(1-cos(asin(nc_open/(2*nc_outer))))));
nc_inner_y = 0;

% -----
% ----- Start Geometry Creation in Femlab -----
% -----

% Define the ellipses based upon the calculated dimensions
g1=ellip2(nc_outer,nc_outer,'base','center','pos', ...
[nc_outer_x,nc_outer_y],'rot','0');
g5=ellip2(nc_inner,nc_inner,'base','center','pos', ...
[nc_inner_x,nc_inner_y],'rot','0');

% Define the environment bound rectangle
bound_rect = rect2('4e-6','2e-6','base','center', ...
'pos',{'0','0'},'rot','0');

% Boolean operations to create the "sharp structures"
sharp_nc = geomcomp({g1,g5},'ns',{'g1','g5'},'sf', ...
'g1-g5','edge','none');

```

```

% Fillets
round_nc = fillet(sharp_nc,'radii',2.5E-10,'point',[1 2]);

% Rotate the finished nanocrescent
nanocrescent = rotate(round_nc, theta ,[0,0]);

clear s
s.objs = {nanocrescent, bound_rect};
s.name={'NC','BR'};
s.tags={'nanocrescent','boundrect'};

fem.draw=struct('s',s);
fem.geom=geomcsg(fem);

% -----
% ----- Start Simulation Loop -----
% -----

% Vector of the max electric field at each wavelength
emax = [];

% The wavelengths we are solving at
lambda = linspace(451e-9,1088e-9,1);

% Generate the dielectric function data
eps_i = OpticalData(451e-9,1088e-9,1,1);
eps_o = 1;

for ii = 1 : length(lambda),
fem.const={'eps_i',eps_i(ii),'eps_o',eps_o};

    clear appl
    appl.mode.class = 'InPlaneWaves';
    appl.module = 'CEM';
    appl.assignsuffix = '_wh';

% Solve via input wavelength

```

```

clear prop
prop.field='TM';
prop.inputvar='lambda';
appl.prop = prop;

% Set the boundary conditions
clear bnd
bnd.H0 = {{0;0;1},{0;0;0},{0;0;0}};
bnd.type = {'NR','cont','NR'};
bnd.ind = [1,3,3,3,2,2,2,2,2,2,2,2,2,2,2];
appl.bnd = bnd;

% Set the domain variables
clear equ
equ.epsilonr = {'eps_o','eps_i'};
equ.ind = [1,2];
appl.equ = equ;

% Set the current wavelength
appl.var = {'nu','1e9','lambda0',lambda(ii)};
fem.appl{1} = appl;
fem.border = 1;

fem=multiphysics(fem);

% Mesh initialize parameters, smaller = finer
fem.mesh=meshinit(fem, ...
    'hmaxfact',.8, ...
    'hcurve',0.15, ...
    'hgrad',1.15, ...
    'hcutoff',0.001);

fem.xmesh=meshextend(fem);

fem.sol=femlin(fem, ...
    'solcomp',{'Hz'}, ...
    'outcomp',{'Hz'});

```

```

% posteval returns the electric field at each point
    eii_struct = posteval(fem,'10*log10(normE_wh/450)', 'dl', [1]);

% Take the maximum field value and add it to emax
    eii_max = max(eii_struct.d);
    emax = [emax eii_max];
end

% Clean up all of our loose ends
save opticalData emax lambda;
clear;
load opticalData;

```

B.2 OpticalFourLayer.m

```

%{
Joseph Doll
OpticalFourLayer.m
FEMLAB 3.1 simulation to calculate the maximum local electric field
enhancement for a four layer gold, iron, silver, gold nanocrescent
of arbitrary ID, OD, layer thickness and opening width in a low
absorption dielectric medium of arbitrary dielectric constant.
%}

flclear fem
clear vrsn
vrsn.name = 'FEMLAB 3.1';
vrsn.ext = '';
vrsn.major = 0;
vrsn.build = 157;
vrsn.rcs = '$Name: $';
vrsn.date = '$Date: 2004/11/12 07:39:54 $';
fem.version = vrsn;

% -----
% ----- Start Geometry Initialization -----
% -----

```

```

% Nominal opening width between tips (increased by fillet)
nc_open = 72e-9;
fe_open = 70e-9;
ag_open = 72e-9;

% Radii of circles that define the nanocrescent layers
nc_outer = 95e-9;
nc_inner = 75e-9;
ag_outer = nc_outer - (5/40)*(nc_outer - nc_inner);
fe_outer = ag_outer - (20/40)*(nc_outer - nc_inner);
fe_inner = fe_outer - (10/40)*(nc_outer - nc_inner);
% Note that the circles will be shifted later, so thicknesses
% here are not exact.

% Calculate the horizontal displacement of each ellipse based
% upon the dimensions noted above (radii and opening widths)
nc_outer_x = 0;
nc_outer_y = 0;

ag_outer_x = -((nc_outer - ag_outer) + ...
(ag_outer*(1-cos(asin(ag_open/(2*ag_outer)))))) - ...
(nc_outer*(1-cos(asin(ag_open/(2*nc_outer))))));
ag_outer_y = 0;

fe_outer_x = -((nc_outer - fe_outer) + ...
(fe_outer*(1-cos(asin(fe_open/(2*fe_outer)))))) - ...
(nc_outer*(1-cos(asin(fe_open/(2*nc_outer))))));
fe_outer_y = 0;

fe_inner_x = -((nc_outer - fe_inner) + ...
(fe_inner*(1-cos(asin(fe_open/(2*fe_inner)))))) - ...
(nc_outer*(1-cos(asin(fe_open/(2*nc_outer))))));
fe_inner_y = 0;

nc_inner_x = -((nc_outer - nc_inner) + ...
(nc_inner*(1-cos(asin(nc_open/(2*nc_inner)))))) - ...
(nc_outer*(1-cos(asin(nc_open/(2*nc_outer))))));

```

```

nc_inner_y = 0;

% -----
% ----- Start Geometry Creation in Femlab -----
% -----

% Define the ellipses based upon the calculated dimensions
g1=ellip2(nc_outer,nc_outer,'base','center','pos', ...
[nc_outer_x,nc_outer_y],'rot','0');
g2=ellip2(ag_outer,ag_outer,'base','center','pos', ...
[ag_outer_x,ag_outer_y],'rot','0');
g3=ellip2(fe_outer,fe_outer,'base','center','pos', ...
[fe_outer_x,fe_outer_y],'rot','0');
g4=ellip2(fe_inner,fe_inner,'base','center','pos', ...
[fe_inner_x,fe_inner_y],'rot','0');
g5=ellip2(nc_inner,nc_inner,'base','center','pos', ...
[nc_inner_x,nc_inner_y],'rot','0');

% Define the environment bound rectangle
bound_rect = rect2('4e-6','2e-6','base','center', ...
'pos',{'0','0'},'rot','0');

% Boolean operations to create the "sharp structures"
sharp_nc = geomcomp({g1,g5},'ns',{'g1','g5'],'sf', ...
'g1-g5','edge','none');
sharp_ag = geomcomp({g2,g3},'ns',{'g2','g3'],'sf', ...
'g2-g3','edge','none');
sharp_fe = geomcomp({g3,g4},'ns',{'g3','g4'],'sf', ...
'g3-g4','edge','none');

% Fillets
round_nc = fillet(sharp_nc,'radii',5.0E-10,'point',[1 2]);
round_ag = fillet(sharp_ag,'radii',3.5E-10,'point',[1 2]);
round_fe = fillet(sharp_fe,'radii',2.5E-10,'point',[1 2]);

% Combine the geometry into a single final structure
nc_struct = geomcomp({round_nc,round_fe,round_ag},'ns', ...

```

```

{'C01','C02','C03'},'sf','C01+C02+C03','edge','none');

% Rotate the finished nanomoon through the angle theta
nanocrescent = rotate(nc_struct, -pi ,[0,0]);

clear s
s.objs = {nanocrescent, bound_rect};
s.name={'NC','BR'};
s.tags={'nanocrescent','boundrect'};

fem.draw=struct('s',s);
fem.geom=geomcsg(fem);

% -----
% ----- Start Simulation Loop -----
% -----

emax = [];

lambda = linspace(451e-9,1088e-9,100);
eps_au = OpticalData(451e-9,1088e-9,100,1);
eps_ag = OpticalData(451e-9,1088e-9,100,2);
eps_fe = OpticalData(451e-9,1088e-9,100,3);
eps_o = 1;

for ii = 1 : length(lambda),
    fem.const={'eps_au',au_eps(ii),'eps_ag',ag_eps(ii), ...
'eps_fe',fe_eps(ii),'eps_o',eps_o};

    clear appl
    appl.mode.class = 'InPlaneWaves';
    appl.module = 'CEM';
    appl.assignsuffix = '_wh';
    clear prop
    prop.field='TM';
    prop.inputvar='lambda';
    appl.prop = prop;
    clear bnd

```

```

    bnd.H0 = {{0;0;0},{0;0;1},{0;0;0}};
    bnd.type = {'cont','NR','NR'};
    bnd.ind = [2,3,3,3 1 1 1 1 1 1 1 1 1 1 1 1 1 1 1 1 1 1 ...
1 1 1 1 1 1 1 1 1 1];
    appl.bnd = bnd;
    clear equ
    equ.epsilonr = {'eps_o','eps_au','eps_ag','eps_fe'};
    equ.mur = {1,1,1,5000};
    equ.ind = [1,2,3,4];
    appl.equ = equ;
    appl.var = {'nu','1e9','lambda0',lambda(ii)};
    fem.appl{1} = appl;
    fem.border = 1;

    fem=multiphysics(fem);

    fem.mesh=meshinit(fem, ...
        'hmaxfact',1.4, ...
        'hgrad',1.2, ...
        'hcurve',0.15, ...
        'hcutoff',0.000001);

    fem.xmesh=meshextend(fem);

    fem.sol=femlin(fem, ...
        'solcomp',{'Hz'}, ...
        'outcomp',{'Hz'});

% posteval returns the electric field at each point
eii_struct = posteval(fem,'10*log10(normE_wh/450)','dl',[1]);

% Take the maximum field value and add it to emax
eii_max = max(eii_struct.d);
emax = [emax eii_max];
end

% Clean up all of our loose ends
save opticalData emax lambda;

```

```
clear;
load opticalData;
```

B.3 OpticalSphere.m

```
%{
Joseph Doll
OpticalSphere.m
FEMLAB 3.1 simulation to calculate the maximum local electric field
enhancement for a gold or silver sphere of arbitrary radius immersed
in a low absorption dielectric medium of arbitrary dielectric constant.
%}

flclear fem
clear vrsn
vrsn.name = 'FEMLAB 3.1';
vrsn.ext = '';
vrsn.major = 0;
vrsn.build = 157;
vrsn.rcs = '$Name: $';
vrsn.date = '$Date: 2004/11/12 07:39:54 $';
fem.version = vrsn;

% -----
% ----- Start Geometry Initialization -----
% -----

% Sphere radius
radius = 75e-9;

% Define the ellipses based upon the calculated dimensions
g5 = ellip2(radius,radius,'base','center','pos',{'0','0'}, ...
'rot','0');

% Define the environment bound rectangle
bound_rect = rect2('4e-6','2e-6','base','center','pos', ...
{'0','0'},'rot','0');
```

```

clear s
s.objs = {g5, bound_rect};
s.name={'SP', 'BR'};
s.tags={'sphere', 'boundrect'};

fem.draw=struct('s',s);
fem.geom=geomcsg(fem);

% Vector of the max electric field at each wavelength
emax = [];

% The wavelengths we are solving at
lambda = linspace(451e-9,1088e-9,41);

% Generate the dielectric function data
eps_i = OpticalData(451e-9,1088e-9,41,1);
eps_o = 1;

% -----
% ----- Start Simulation Loop -----
% -----

% Iterate and simulate at each wavelength
for ii = 1 : length(lambda),
fem.const={'eps_i',eps_i(ii),'eps_o',eps_o};

clear appl
appl.mode.class = 'InPlaneWaves';
appl.module = 'CEM';
appl.assignsuffix = '_wh';
clear prop
prop.field='TM';
prop.inputvar='lambda';
appl.prop = prop;
clear bnd
bnd.H0 = {{0;0;0},{0;0;1},{0;0;0}};
bnd.type = {'cont', 'NR', 'NR'};

```

```

bnd.ind = [2,3,3,3,1,1,1,1];
appl.bnd = bnd;
clear equ
equ.epsilonr = {'eps_o','eps_i'};
equ.ind = [1,2];
appl.equ = equ;
appl.var = {'nu','1e9','lambda0',lambda(ii)};
fem.appl{1} = appl;
fem.border = 1;

% Multiphysics
fem=multiphysics(fem);

% Initialize mesh
fem.mesh=meshinit(fem, ...
    'hmaxfact',.3, ...
    'hcurve',0.15, ...
    'hgrad',1.1, ...
    'hcutoff',0.001);

% Extend mesh
fem.xmesh=meshextend(fem);

% Solve problem
fem.sol=femlin(fem, ...
    'solcomp',{'Hz'}, ...
    'outcomp',{'Hz'});

% posteval returns the electric field at each point
eii_struct = posteval(fem,'10*log10(normE_wh/450)','dl',[1]);

% Take the maximum field value and add it to emax
eii_max = max(eii_struct.d);
emax = [emax eii_max];
end

% Clean up all of our loose ends
save opticalData emax lambda;

```

```
clear;
load opticalData;
```

B.4 Magnetic2d.m

```
%{
Joseph Doll
Magnetic2d.m
2D FEMLAB 3.1 simulation to calculate the torque experienced by a
four layer au/fe/ag/au nanocrescent subjected to a magnetic field
field on the order of .1T.
%}

flclear fem
clear vrsn
vrsn.name = 'FEMLAB 3.1';
vrsn.ext = '';
vrsn.major = 0;
vrsn.build = 157;
vrsn.rcs = '$Name: $';
vrsn.date = '$Date: 2004/11/12 07:39:54 $';
fem.version = vrsn;

% Width of opening aperture of the gold shell and iron core
AuOpenWidth = 70e-9;
MagOpenWidth = 72e-9;

R1 = 50e-9; % Outer arc of gold shell
R2 = 80e-9; % Outer arc of magnetic core
R3 = 75e-9; % Inner arc of magnetic core
R4 = 20e-9; % Inner arc of gold shell

x1 = 0;
y1 = 0;

x2 = 0;
y2 = -((R1-R2) + (R2*(1-cos(asin(MagOpenWidth/(2*R2)))))) ...
```

```

        - (R1*(1-cos(asin(MagOpenWidth/(2*R1))))));
x3 = 0;
y3 = -((R1-R3) + (R3*(1-cos(asin(MagOpenWidth/(2*R3)))))) ...
    - (R1*(1-cos(asin(MagOpenWidth/(2*R1))))));

% Mass and Center of Mass Calculations:

% Densities of core and shell, kg/m^3
rhoCore = 5170;
rhoShell = 19320;

% Approx. volumes of core and shell, m^3
volumeCore = 4/3*pi*(R2^3-R3^3);
volumeShell = 4/3*pi*(R1^3-R2^3+R3^3-R4^3);

% Masses of core and shell, kg
massCore = rhoCore * volumeCore;
massShell = rhoShell * volumeShell;

% Center of mass of core
cmCore = (4/3*pi*(R2^3*y2 - R3^3*y3)*rhoCore)/massCore;

% Iron (Fe) Core
murCore = 5e3;

% Magnetization of the plate in the +y axis
magPlate = 1/(4*pi*1e-7);

fem.const = {'magPlate',magPlate,'murCore',murCore, ...
'cmCore',cmCore};

torqueZ = [];

for theta = linspace(0,pi,5),

    g2=ellip2(R2,R2,'base','center','pos',[x2,y2],'rot','0');

```

```

g3=ellip2(R3,R3,'base','center','pos',[x3,y3],'rot','0');

% Define the environment bound rectangle
bound = rect2('8e-7','8e-7','base','center','pos', ...
{'0','-2e-7'],'rot','0');

% Define the magnetic field plates
botPlate=rect2('.5E-6','1.0E-7','base','center','pos', ...
{'0','-180E-9'],'rot','0');

% Subtraction
g6=geomcomp({g2,g3},'ns',{'g2','g3'],'sf','g2-g3', ...
'edge','none');

% Fillets
g8=fillet(g6,'radii',.25e-9,'point',[3 6]); % Inner radii

nanomoon=rotate(g8,theta,[0,cmCore]);

clear s
s.objs={nanomoon,bound,botPlate};
s.name={'NM','BD','BP'};
s.tags={'nanomoon','bound','botPlate'};

fem.draw=struct('s',s);
fem.geom=geomcsg(fem);

% ----- Solve -----

clear appl
appl.mode.class = 'PerpendicularCurrents';
appl.module = 'CEM';
appl.assignsuffix = '_qa';

clear prop
prop.elemdefault='Lag1';
appl.prop = prop;

```

```

clear bnd
bnd.type = {'A0'};
appl.bnd = bnd;

clear equ
equ.mur = {1,0,'murCore'};
equ.magconstrel = {'mur','M','mur'};
equ.M = {{0;0},{0;'magPlate'},{0;0}};
equ.L = {1,1,150e-9};

% Name the maxwell stress tensor on the magnetic
% core surface
equ.maxwell = {{},{},'coreForce'};
equ.ind = [1,2,3];
appl.equ = equ;

fem.appl{1} = appl;
fem=multiphysics(fem);

fem.mesh=meshinit(fem, ...
    'hmaxfact',0.15, ...
    'hgrad',1.1, ...
    'hcurve',0.2, ...
    'hcutoff',0.0001);

fem.xmesh=mesnextend(fem);

fem.sol=femlin(fem, ...
    'solcomp',{'Az'}, ...
    'outcomp',{'Az'});

% Integrate each infinitesimal contribution of
% the Maxwell stress tensor about the core
% center of mass along the appropriate boundaries
tZ = postint(fem,'x*coreForce_nTy_qa - ...
(y-cmCore)*coreForce_nTx_qa','edim',1,'dl',[9:18]);
torqueZ = [torqueZ tZ];
end

```

B.5 Magnetic3d.m

```
%{
Joseph Doll
Magnetic2d.m
3D FEMLAB 3.1 simulation to calculate the torque experienced by a
magnetic core that is sandwiched between an au and ag layer in a
composite four layer nanocrescent. Magnetic core is subjected to
a magnetic field on the order of .1T.
%}

flclear fem
clear vrsn
vrsn.name = 'FEMLAB 3.1';
vrsn.ext = '';
vrsn.major = 0;
vrsn.build = 157;
vrsn.rcs = '$Name: $';
vrsn.date = '$Date: 2004/11/12 07:39:54 $';
fem.version = vrsn;

% The diameter of the circular opening into the nanomoon.
% The core is embedded within the shell
ShellOpenWidth = 70e-9; % Shell is gold
CoreOpenWidth = 72e-9; % Core is iron oxide (hematite)

% Radii of the spheres that generate the nanomoon structure
R1 = 50e-9; % Outer arc of gold shell
R2 = 80e-9; % Outer arc of magnetic core
R3 = 75e-9; % Inner arc of magnetic core
R4 = 25e-9; % Inner arc of gold shell

% Density values
rhoCore = 5170; % Density of core, kg/m3
rhoShell = 19320; % Density of gold, kg/m3

% -----
% ----- Magnetic Parameters -----
```

```

% -----
% Magnetic permeability (relative)
murShell = .99996; % Gold shell
murCore = 5e3; % Iron Oxide (Fe2O3) Core

% Magnetization of the plate in the +z axis
magPlate = 1/(4*pi*1e-7);

% -----
% -----

% Volume calculations
volumeCore = 4/3*pi*(R2^3-R3^3); % Volume of the magnetic core
volumeShell = 4/3*pi*(R1^3-R2^3+R3^3-R4^3); % Volume of the shell

% Mass calculations
massCore = rhoCore * volumeCore; % Mass of the core
massShell = rhoShell * volumeShell; % Mass of the shell

% Calculate the vertical displacement of each ellipse based upon
% the dimensions noted above (radii and opening widths)
x1 = 0;
y1 = 0;
z1 = 0;

x2 = 0;
y2 = 0;
z2 = -((R1-R2) + (R2*(1-cos(asin(CoreOpenWidth/(2*R2)))))) ...
      - (R1*(1-cos(asin(CoreOpenWidth/(2*R1))))));

x3 = 0;
y3 = 0;
z3 = -((R1-R3) + (R3*(1-cos(asin(CoreOpenWidth/(2*R3)))))) ...
      - (R1*(1-cos(asin(CoreOpenWidth/(2*R1))))));

x4 = 0;
y4 = 0;
z4 = -((R1-R4) + (R4*(1-cos(asin(ShellOpenWidth/(2*R4)))))) ...

```

```

- (R1*(1-cos(asin(ShellOpenWidth/(2*R1))))));

% The z-component of the coordinate of the center of
% mass of the core
cmCore = (4/3*pi*(R2^3*z2 - R3^3*z3)*rhoCore)/massCore;

% Output data vectors. Initialized to be empty.
torqueX = [];
torqueY = [];
torqueZ = [];

forceZ = [];

% Rotate the geometry to each angle theta (radians) and solve
for theta = linspace(0,pi,5),

    % Constants that accesible in Femlab
    fem.const={'magPlate',magPlate,'murShell',murShell, ...
'murCore',murCore,'cmCore',cmCore};

    % Define the ellipses based upon the calculated dimensions
    %g1=sphere3(R1,'pos',[x1,y1,z1],'axis', ...
{'0','0','1'},'rot','0');
    g2=sphere3(R2,'pos',[x2,y2,z2],'axis', ...
{'0','0','1'},'rot','0');
    g3=sphere3(R3,'pos',[x3,y3,z3],'axis', ...
{'0','0','1'},'rot','0');
    %g4=sphere3(R4,'pos',[x4,y4,z4],'axis', ...
{'0','0','1'},'rot','0');

    % Define the environment bound block
    Bound=block3('1.5E-6','1.5E-6','1E-6','base','center', ...
'pos',{'0','0','0'},'axis',{'0','0','1'},'rot','0');

    % Define the magnetic field plates
    Plate=block3('1E-6','1E-6','1E-7','base','center', ...
'pos',{'0','0','-2.0E-7'},'axis',{'0','0','1'},'rot','0');

```

```

% Subtraction
%g5=geomcomp({g1,g4},'ns',{'g1','g4'],'sf', ...
'g1-g4','face','none','edge','all');
g6=geomcomp({g2,g3},'ns',{'g2','g3'],'sf', ...
'g2-g3','face','none','edge','all');

% Combine the geometry into a single final structure
%nanomoon1=geomcomp({g5,g6},'ns',{'C01','C02'],'sf', ...
'C01+C02','face','none','edge','all');

% Rotate the nanocrescent through the angle theta about the y-axis
Nanomoon=rotate(g6, theta , [0,1,0] , [0,0,cmCore] );

% Designate the final components

clear s
s.objs={Nanomoon,Bound,Plate};
s.name={'NM','BD','P'};
s.tags={'Nanomoon','Bound','Plate'};

fem.draw=struct('s',s);
fem.geom=geomcsg(fem);

clear appl
appl.mode.class = 'MagnetostaticsNoCurrents';
appl.module = 'CEM';
appl.assignsuffix = '_nc';

clear bnd
bnd.type = {'cont','nB0','Vm0'};
bnd.murbnd = {0,1,1};
bnd.ind = [2,2,2,3,2,1,1,1,1,1,1,1,1,1,1,1, ...
1,1,1,1,1,1,1,1,1,1,1,2];
appl.bnd = bnd;

clear equ
equ.mur = {1,1,'murCore'};
equ.magconstrel = {'mur','M','mur'};

```

```

equ.M = {{0;0;0},{0;0;'magPlate'},{0;0;0}};
equ.maxwell = {{},{},'coreForce'};
equ.ind = [1,2,3];
appl.equ = equ;
fem.appl{1} = appl;
fem.border = 1;

fem=multiphysics(fem);

fem.mesh=meshinit(fem, ...
    'hmaxfact',1.2, ...
    'hcutoff',.01, ...
    'hgrad',1.4, ...
    'hcurve',0.25); %, ...
    '%hnarrow',2, ... // Resolution in narrow regions
    '%hpnt',100, ... // Resolution of geometry
    '%xscale',5, ... // Scale factor for scale, mesh, revert process
    '%yscale',5, ...
    '%zscale',5);

% Extend mesh
fem.xmesh=meshextend(fem);

% Solve problem (Conjugate Gradients, SSOR, Symmetric Matrices)
% Suitable for large scale 3d models with symmetric matrices
fem.sol=femlin(fem, ...
    'conjugate','off', ...
    'symmetric','on', ...
    'solcomp',{'Vm'}, ...
    'outcomp',{'Vm'}, ...
    'linsolver','cg',...
    'prefun','ssor');

% Calculate the torque and force vectors on the
% magnetic core and append them to their respective vectors.

% Torque, x component
tX=postint(fem,'y*coreForce_nTz_nc - (z-cmCore)* ...

```

```

coreForce_nTy_nc','edim', 2,'d1',[11:26]);
torqueX = [torqueX tX];
% Torque, y component
tY=postint(fem,'(z-cmCore)*coreForce_nTx_nc - x* ...
coreForce_nTz_nc','edim', 2,'d1',[11:26]);
torqueY = [torqueY tY];

% Torque, z component
tZ=postint(fem,'x*coreForce_nTy_nc - y* ...
coreForce_nTx_nc','edim', 2,'d1',[11:26]);
torqueZ = [torqueZ tZ];

% Force, z component
fZ = posteval(fem, 'coreForce_forcez_nc','edim', 0);
fZ = fZ.d(1);
forceZ = [forceZ fZ];

end

save magCoreData torqueX torqueY torqueZ forceZ;
clear
load magCoreData

```

Bibliography

- [1] Liu G.L. Kim J. Mejia Y.X. & Lee L.P. Lu, Y. Nanophotonic crescent moon structures with sharp edge for ultrasensitive biomolecular detection by local electromagnetic field enhancement effect. *Nano Lett.*, 5:119–124, 2005.
- [2] K. et al. Kneipp. Extremely large enhancement factors in surface-enhanced raman scattering for molecules on colloidal gold clusters. *Appl Spectrosc*, 52:1493–1497, 1998.
- [3] A. Bizzarri and S. Cannistraro. Surface-enhanced resonance raman spectroscopy signals from single myoglobin molecules. *Appl. Spec*, 56:1531–1537, 2002.
- [4] D. Graham et al. Simple multiplex genotyping by surface-enhanced resonance raman scattering. *Anal. Chem.*, 74:1069–1074, 2002.
- [5] B. Moore et al. Rapid and ultra-sensitive determination of enzyme activities using surface-enhanced resonance raman scattering. *Nature Biotech*, 22:1133–1138, 2004.
- [6] N. J. Halas P. Nordlander. E. Prodan, C. Radloff. Hybridization model for the plasmon response of complex nanostructures. *Science*, 302:419, 2003.
- [7] N. Halas et al. S. Oldenburg. Nanoengineering of optical resonances. *Chem. Phys. Lett.*, 288:243, 1998.
- [8] N. Halas. J. Jackson. Silver nanoshells: Variations in morphologies and optical properties. *J. Phys. Chem. B.*, 105:2743, 2001.
- [9] J. West et al. J. Barton, N. J. Halas. Nanoshell-enabled photonics-based imaging and therapy of cancer. *Tech. Cancer Res. Trtmnt*, 1:33, 2004.
- [10] C. Moran F. Tam and N. Halas. Geometrical parameters controlling sensitivity of nanoshell plasmon resonances to changes in dielectric environment. *J. Phys. Chem. B*, 108:17290–17294, 2004.

- [11] C. Nehl et al. Scattering spectra of single gold nanoshells. *Nano Lett*, 4:2355–2359, 2004.
- [12] E. Bohn. W. Stober, A. Fink. Controlled growth of monodisperse silica spheres in the micron size range. *J. Coll. Infrfc. Sci.*, 26:62, 1968.
- [13] Westcott S.L. Averitt R.D. & Halas N.J. Oldenburg, S.J. Surface enhanced raman scattering in the near infrared using metal nanoshell substrates. *J Chem Phys*, 111:4729–4735, 1999.
- [14] L. R. Hirsch J. L. West J. B. Jackson, S. L. Westcott and N. J. Halas. Controlling the surface enhanced raman effect via the nanoshell geometry. *Applied Physics Letters*, 82:257, 2003.
- [15] J. et al. Aizpurua. Optical properties of gold nanorings. *Phys Rev Lett*, 90, 2003.
- [16] Michael Stroschia and ed. Mitra Dutta. *Biological Nanostructures and Applications of Nanostructures in Biology: Electrical, Mechanical & Optical Properties*. Kluwer Academic / Plenum Publishers, New York, 2004.
- [17] Dubertret et al. In vivo imaging of quantum dots encapsulated in phospholipid micelles. *Science*, 298:1759–1762, 2002.
- [18] C.V. Raman. A change of wavelength in light scattering. *Nature*, 121:619, 1928.
- [19] K. et al. Kneipp. Surface enhanced raman spectroscopy in single living cells using gold nanoparticles. *Appl. Spectr.*, 56:150–154, 2002.
- [20] K. et al. Kneipp. Single molecule detection using surface enhanced raman scattering (sers). *Phys Rev Lett*, 78:1667–1670, 1997.
- [21] S.M. Nie and S.R. Emery. Probing single molecules and single nanoparticles by surface enhanced raman scattering. *Science*, 275:1102–1106, 1997.
- [22] A. Haka et al. Diagnosing breast cancer by using raman spectroscopy. *Biophysics*, 102:12371–12376, 2005.
- [23] P.J. Hendra M. Fleischmann and A. J. Mac Quillan. Raman spectra of pyridine adsorbed at a silver electrode. *Chem. Phys. Lett.*, 26:162, 1974.
- [24] A. Campion and P. Kambhampati. Surface-enhanced raman scattering. *Chem. Soc. Rev*, 27:241–250, 1998.

- [25] J.B. GarciaVidal, F.J. & Pendry. Collective theory for surface enhanced raman scattering. *Phys Rev Lett*, 77:1163–1166, 1996.
- [26] S. Sarkar. *Molecular Models of Life: Philosophical Papers on Molecular Biology*. MIT Press, Cambridge, 2005.
- [27] J. Albala and ed. Ian Humphery-Smith. *Protein Arrays, Biochips and Proteomics: The Next Phase of Genomic Discovery*. Marcel Dekker, New York, 2003.
- [28] Craig Bohren and Donald Huffman. *Absorption and scattering of light by small particles*. 1983.
- [29] A Review of Elastic Light Scattering Theories. Thomas wriedt. *Part. Part. Syst. Charact.*, 15:67–74, 1998.
- [30] B. Lamprecht et al. Metal nanoparticle gratings: Influence of dipolar particle interaction on the plasmon resonance. *Phys. Rev. Lett.*, 84:4721–4724, 2000.
- [31] P. B. Johnson and R. W. Christy. Optical constants of the noble metals. *Phys. Rev. B*, 6:4370–4379, 1972.
- [32] ed. Boardman, A.D. *Electromagnetic Surface Modes (Ch. 9)*. John Wiley & Sons, New York, 1982.
- [33] U. Kreibig and Michael Vollmer. *Optical Properties of Metal Clusters*. Springer-Verlag, Berlin, 1995.
- [34] H. Atwater. Guiding light. *OE Magazine*, July 2002.
- [35] J. Li. Investigation of application for surface plasmon resonance (master’s thesis). *U. Washington*, 2004.
- [36] R. H. Ritchie. Plasma losses by fast electrons in thin films. *Phys. Rev.*, 106:874–881, 1957.
- [37] H. Raether. *Surface Plasmons*. Springer, Berlin, 1988.
- [38] T. Ebbesen. W. Barnes, A. Dereux. Surface plasmon subwavelength optics. *Nature*, 424:824–830, 2003.
- [39] M.J. Weber. *Handbook of Optical Materials*. CRC Press, Boca Raton, 2003.

- [40] J. Kim J. C. Doll G. L. Liu, Y. Lu and L. P. Lee. Composite nanocrescent raman probes for function in vivo nanospectroscopy. *Submitted, not published*, 2005.
- [41] Liu G. L. Lu Y. & Lee L. P. Kim, J. Local field enhancement in nanoscale crescent structures by coupling and hybridization of tip and cavity surface plasmon resonances. *Submitted, not published*, 2005.
- [42] B. Choi and G. Zocchi. Artificial allosteric control of maltose binding protein. *Phys. Rev. Lett.*, 94:038103, 2005.
- [43] J.J. Diao and G.D. Chen. Electromagnetic cavity resonant absorption of the gold nanoshell. *J. Phys. D: Appl. Phys.*, 34:24592–6, 2001.
- [44] J. C. Weeber et al. Plasmon polaritons of metallic nanowires for controlling submicron propagation of light. *Phys. Rev. B*, 60:9061–9068, 1999.
- [45] B. Grzybowski et al. Dynamic self-assembly of magnetized, millimetre-sized objects rotating at a liquid-air interface. *Nature*, 405:1033–1036, 2000.
- [46] R. Anker, J.N. & Kopelman. Magnetically modulated optical nanoprobe. *Appl Phys Lett*, 82:1102–1104, 2003.
- [47] S. Yee J. Homola and G. Gauglitz. Surface plasmon resonance sensors: review. *Sens. Act. B*, 54:3–15, 1999.
- [48] M. Piliarik et al. A new surface plasmon resonance sensors for high-throughput screening applications. *Biosens. Bioelect.*, 25:2104–2110, 2005.
- [49] J. Shumaker-Parry et al. Parallel, quantitative measurement of protein binding to a 120-element double-stranded dna array in real time using surface plasmon resonance microscopy. *Anal. Chem.*, 76:2071–2082, 2004.